Annex 4G: Near Detector Reference Design

LBNF/DUNE Conceptual Design Report (DRAFT)

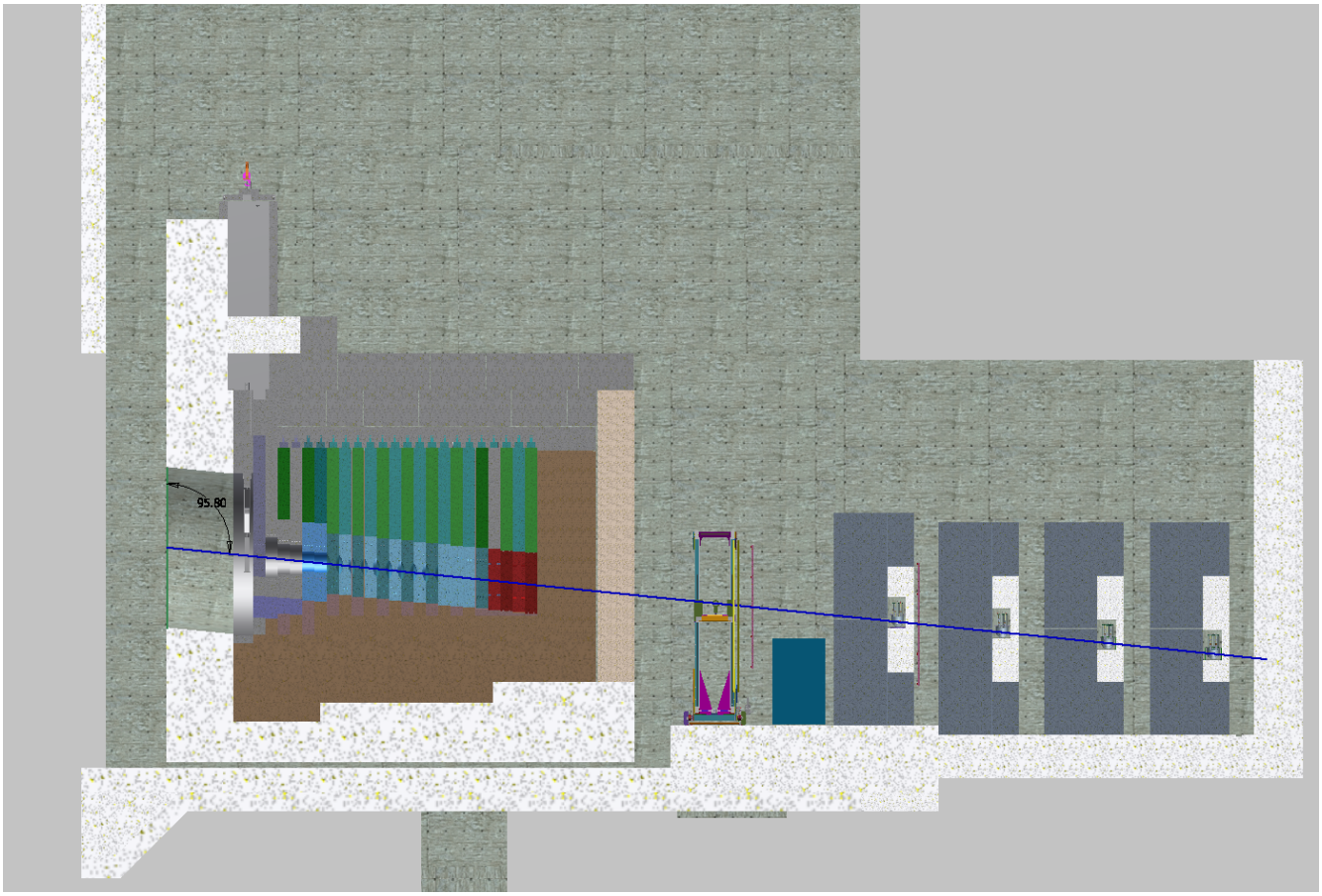

May 22, 2015

Contents

Acronyms, Abbreviations and Units **iv**

1 Introduction **1**

2 The Near Neutrino Detector: A Fine-Grained Tracker **3**
2.1 Introduction . . . 3
2.2 Motivation . . . 3
2.3 Overview of FGT Design . . . 4
2.4 Straw-Tube Tracking Detector . . . 6
2.4.1 Straw Tubes . . . 6
2.4.2 Radiator Targets . . . 8
2.4.3 Argon, Water, and Other Nuclear Targets . . . 9
2.5 Electromagnetic Calorimeter . . . 9
2.6 Dipole Magnet . . . 12
2.7 Muon Identifier . . . 12
2.8 FGT Instrumentation . . . 16
2.8.1 Readout Electronics . . . 16
2.8.2 Humidity and Temperature Monitoring . . . 17
2.8.3 Gas Leak Monitoring in the STT and MuID . . . 19
2.8.4 Magnet Monitoring . . . 19

3 Near Detector Beamline Measurements **20**
3.1 Introduction . . . 20
3.2 Design Considerations . . . 20
3.2.1 General . . . 20
3.2.2 Muon Measurements . . . 21
3.3 Muon-Measurement Facilities . . . 23
3.4 Muon Cherenkov Detectors . . . 26
3.4.1 Introduction . . . 26
3.4.2 Reference Design . . . 27
3.4.3 Prototype Development and Testing . . . 29
3.4.4 Installation . . . 29
3.4.5 Operation . . . 32
3.5 Muon-Ionization Measurements . . . 32
3.5.1 Introduction . . . 32
3.5.2 Reference Design . . . 32

3.5.3 Prototype Design and Testing . . . 35
3.5.4 Installation . . . 35
3.5.5 Operation . . . 35
3.6 Stopped-Muon Detector . . . 36
3.6.1 Introduction . . . 36
3.6.2 Reference Design . . . 37
3.6.3 Prototype Development and Testing . . . 37
3.6.4 Installation . . . 39
3.6.5 Operation . . . 39

4 Data Acquisition and Computing for the Near Detector System 40
4.1 NDS DAQ . . . 40
4.1.1 NDS Master DAQ . . . 40
4.1.2 Near Neutrino Detector DAQ (NND-DAQ) . . . 41
4.1.3 Beamline Measurements DAQ (BLM-DAQ) . . . 42
4.2 NDS Computing . . . 43

5 Measurements at External Facilities 44
5.1 Introduction . . . 44
5.2 External Neutrino-Beam Measurements . . . 44
5.3 External Hadron-Production Measurements . . . 44
5.3.1 Background . . . 45
5.3.2 Strategy . . . 46
5.3.3 Use of External Facilities for Measurements . . . 46
5.4 The US-NA61/SHINE Program . . . 47

Acronyms, Abbreviations and Units

ADC	analog-to-digital converter
ASIC	application-specific integrated circuit
B-GDAQ	beamline global data acquisition
BEB	back-end board
BLM	beamline-measurement system
CC	charged current (interaction)
CCQE	charged current quasi-elastic (interaction)
CERN	European Organization for Nuclear Research
CNGS	Neutrino Beam to Gran Sasso (at CERN)
DAQ	data acquisition
DUNE	Deep Underground Neutrino Experiment
ECAL	electromagnetic calorimeter
ESH	Environment, Safety and Health
eV	electron-Volt, unit of energy (also keV, MeV, GeV, etc.)
FEB	front-end board
FGT	Fine-Grained Tracker
FPGA	field-programmable gate array
FRA	Fermi Research Alliance

g-2	the New Muon g-2 Experiment at Fermilab
GDAQ	global data acquisition
GPS	Global Position System
HEP	high energy physics
ICARUS	Imaging Cosmic And Rare Underground Signals (experiment at LNGS)
K2K	"From KEK to Super–Kamiokande," long-baseline neutrino-oscillation experiment
LANL	Los Alamos National Laboratory
LAr	liquid argon
LAr-FD	(LBNE) Liquid Argon Far Detector
LArTPC	Liquid Argon Time Projection Chamber
LArTPCT	Liquid Argon Time Projection Chamber Tracker system
LBNF	Long-Baseline Neutrino Facility
LHC	Large Hadron Collider (at CERN)
LNGS	Gran Sasso National Laboratory
m	meter (also nm, micron, mm, cm, km)
M-GDAQ	master global data acquisition
MicroBooNE	A 100-ton LArTPC located along Fermilab's Booster neutrino beamline
MINERvA	A neutrino-scattering experiment that uses the NuMI beamline at Fermilab
MiniBooNE	Booster Neutrino Experiment (at Fermilab)
MINOS	Main Injector Neutrino Oscillation Search experiment at Fermilab
MIPP	Main Injector Particle Production Experiment (at Fermilab)
MPPC	multi-pixel photon counter
MuID	muon-identification detector

N-GDAQ	neutrino global data acquisition
NA61	NA61/SHINE, experiment at CERN that studies hadron production in hadron-nucleus and nucleus-nucleus collisions
NC	neutral current (interaction)
ND	(Near Site) neutrino detector
NDS	Near Detector Systems; refers to the L2 Project under LBNE
NOMAD	Neutrino Oscillation Magnetic Detector, experiment at CERN
NOvA	NuMI Off-Axis Neutrino Appearance experiment at Fermilab
NuMI	Neutrino beam to MINOS
PMT	photomultiplier tube
QE	quasi-elastic (interaction)
STT	straw-tube tracker
Super-K	Super-Kamiokande, a neutrino detector in Japan
T	Tesla; unit of magnetic field strength
T2K	Tokai-to-Kamioka, a long-baseline neutrino oscillation experiment in Japan
T2K ND280	Near Detector of the Tokai-to-Kamioka (T2K) experiment, located 280m from the beamline target
TDC	time-to-digital converter
TFB	T2K front-end board
TPC	time projection chamber
TR	transition radiation
TRIP-t	Trigger and Pipeleine with timing (full custom ASIC designed at Fermilab)
UA1	Experiment at CERN that ran from 1986 to 1993
UV	ultra-violet
V	Volt

W	watt (also mW, kW, MW)
WBS	Work Breakdown Structure
WLS	wavelength shifter

List of Figures

2.1 A schematic drawing of the fine-grained tracker design . . . 5
2.2 A schematic drawing of a STT module . . . 7
2.3 Schematic drawing of the water or pressurized-argon targets . . . 9
2.4 Schematic drawing of the ECAL . . . 11
2.5 Side view of the ECAL inside magnet . . . 12
2.6 Schematic drawing of a magnet half-assembly . . . 14
2.7 Schematic drawing of an end-RPC tray . . . 14
2.8 Schematic drawing of an RPC . . . 15
2.9 A schematic drawing of the VMM2 circuit . . . 18

3.1 Simulated neutrino fluxes at Far Detector . . . 22
3.2 Ratio of the flux on-axis to the flux 0.4 mrad off-axis . . . 22
3.3 The Absorber Hall elevation view . . . 24
3.4 The Absorber Hall . . . 24
3.5 Absorber conceptual design, elevation view . . . 25
3.6 Energy loss in absorber . . . 26
3.7 Simulated electron and muon velocities upon exiting absorber . . . 27
3.8 Simulated electron and muon angles upon exiting absorber . . . 28
3.9 [Cherenkov counter design . . . 28
3.10 Muon gas Cherenkov counter . . . 30
3.11 Muon gas Cherenkov counter . . . 31
3.12 Model of ionization detector layout . . . 33
3.13 Model of ionization detector array . . . 34
3.14 ionization detector performance for cross-with-corners layout . . . 34
3.15 Michel-electron detector conceptualization . . . 36
3.16 Absorber conceptual design, elevation view . . . 38

4.1 Near Detector System DAQ block diagram . . . 41
4.2 A block diagram of the Near Neutrino Detector DAQ . . . 42

5.1 A schematic drawing of the CERN NA61 detector . . . 47
5.2 The 2015 run plan for US-NA61. . . . 48

List of Tables

2.1 A summary of the performance for the FGT configuration 5
2.2 Specifications for the FGT 6
2.3 Straw Tube Detector specifications 8
2.4 ECAL specifications 10
2.5 Dipole Magnet specifications 13
2.6 MuID specifications 16
2.7 Number of electronics channels for each of the three detector systems 16

Chapter 1

Introduction

DUNE collaborators have prepared this detailed design document which describes the reference design for the DUNE Near Detector Systems (NDS) and serves as an annex to the more abbreviated discussion in the DUNE CDR. The NDS design pulls heavily from both the LBNE near detector design of March 2012, before the LBNE reconfiguration effort eliminated this detector from the project scope, and from the design proposed by Indian collaborators in their DPR of late 2013.

The role of the DUNE Near Detector Systems (NDS) is to minimize the systematic uncertainties of the long-baseline oscillation program and to thus maximize the oscillation-physics potential of the Far Detector. It is important that the Near Detectors improve the sensitivity of the DUNE long-baseline neutrino-oscillation measurements. The enhanced sensitivity they provide will aid in both the analysis of electron-neutrino appearance, the primary oscillation channel, and muon-neutrino disappearance.

The NDS is made up of the following components:

- Fine-Grained Tracker (FGT) near neutrino detector
- Beamline Measurement System
- Near Detector System Data Acquisition system
- External Measurements

The DUNE Fine-Grained Tracker (FGT) near detector consists of a straw-tube tracking detector (STT) and electromagnetic calorimeter (ECAL) inside of a 0.4-T dipole magnet. In addition, Muon Identifiers (MuIDs) are located in the steel of the magnet, as well as upstream and downstream of the STT. The FGT is designed to make precision measurements of the neutrino fluxes, cross sections, signal rates and background rates.

The Beamline Measurement System (BLM) will be located in the region of the Absorber Complex at the downstream end of the decay region to measure the muon fluxes from hadron decay. The

absorber itself is part of the LBNF Beamline. The BLM is intended to determine the neutrino fluxes and spectra and to monitor the beam profile on a spill-by-spill basis, and will operate for the life of the experiment.

The Near Detector System Data Acquisition system (NDS-DAQ) collects raw data from each NDS detector's individual DAQ, issues triggers, adds precision timing data from a global positioning system (GPS), and builds events. The NDS-DAQ is made up of three parts: NDS Master DAQ (NDS-MDAQ), the Beamline Measurements DAQ (BLM-DAQ) and the Near Neutrino Detector DAQ (NND-DAQ).

In addition, external pion producion measurements will improve the simulation of neutrino fluxes.

Chapter 2

The Near Neutrino Detector: A Fine-Grained Tracker

2.1 Introduction

The DUNE Fine-Grained Tracker (FGT) near neutrino detector consists of a straw-tube tracking detector (STT) and electromagnetic calorimeter (ECAL) inside of a 0.4 T dipole magnet. In addition, Muon Identifiers (MuIDs) are located in the steel of the magnet, as well as upstream and downstream of the STT. The FGT is designed to make precision measurements of the neutrino fluxes, cross sections, signal rates and background rates. This document presents the FGT design, which will meet the physics goals and sensitivities of the DUNE experiment.

2.2 Motivation

In order for DUNE to achieve the desired neutrino-oscillation sensitivity, the charged-current signal events and neutral-current background events in the DUNE far detector (FD) must be precisely predicted as a function of the parameters and variables that affect oscillations. These include energy, leading lepton (which tags the neutrino flavor) and the momentum and identification of particles generated by neutrino interactions. At the FD, the first and the second oscillation maxima signals occur at about 2.4 GeV and 0.8 GeV, respectively — an energy regime where neutrino cross sections and fluxes have large uncertainties. It is therefore crucial to measure the unoscillated neutrino fluxes and their interactions at the near site.

In addition to the oscillation signal, it is critical to identify and measure processes such as neutral current π^0 production, that can mimic oscillation signals at the FD. Thus, the principal focus of the near neutrino detector will be on the neutrino-oscillation energy range of $E_\nu < 8$ GeV, as well as higher neutrino energies that produce background to the oscillation signal. Furthermore, the $8 < E_\nu < 20$ GeV energy range can be used as a "control region", i.e. a region in which to search

for physics beyond the PMNS matrix. Clearly, the measurements must be comparable to those made in the FD, for which the target material is liquid argon (LAr).

Finally, the near neutrino detector must measure nuclear effects, including short-range correlations, two-body currents, pion absorption, initial-state interactions, and final-state interactions. These nuclear effects have an impact on neutrino cross sections and energy determinations, and differences between neutrinos and antineutrinos must be fully understood when searching for CP violation.

The proposed detector will constrain the systematic uncertainties in the DUNE oscillation measurements. Regardless of the process under study, the goal is to have the systematic error less than the corresponding statistical error. The design presented here is the subject of study within the DUNE Science Collaboration. As these studies progress, the design of the DUNE near neutrino detector, referred to as the Fine Grained Tracker (FGT) in this document, may evolve from what is described here.

2.3 Overview of FGT Design

A schematic drawing of the FGT design is shown in Figure 2.1. The fine-grained tracker will measure the neutrino event rates and cross sections on argon, water, and other nuclear targets for both ν_e and ν_μ charged current (CC) and neutral current (NC) scattering events. The FGT design consists of a straw-tube tracker (STT), consisting of straw tubes, water targets, argon targets, and radiator targets, and an electromagnetic calorimeter (ECAL), both inside a dipole magnet. In addition, muon detectors (MuID) consisting of resistive plate chambers (RPCs) will be embedded in the steel of the magnet.

The FGT has excellent position and angular resolutions due to its low-density (~ 0.1 g/cm^2) and high-precision STT. This high resolution is important for determining the neutrino vertex and determining whether the neutrino interaction occurs in the water or argon target. The proposed $3.5 \times 3.5 \times 6.4$ m^3 STT position inside the dipole magnet with magnetic field $B = 0.4$ T will enable particle tracking. The nominal active volume of the STT corresponds to 8 tonnes (metric tons, t) of mass, which is mostly due to the STT targets and radiators. Table 2.1 summarizes the performance for the FGT configuration, and Table 2.2 lists the specifications for the FGT.

For a 120-GeV proton beam, the neutrino event rates in the detector will be $\sim 0.35 \times 10^{-14}$ events/tonne/proton on target. Assuming 0.5×10^{14} protons per beam spill, this corresponds to ~ 1.5 events per spill in the 8-t active volume of the FGT design. Overlaps between interactions are expected to be manageable thanks to the nanosecond-level timing of the FGT relative to the ~ 10-μs beam-spill length.

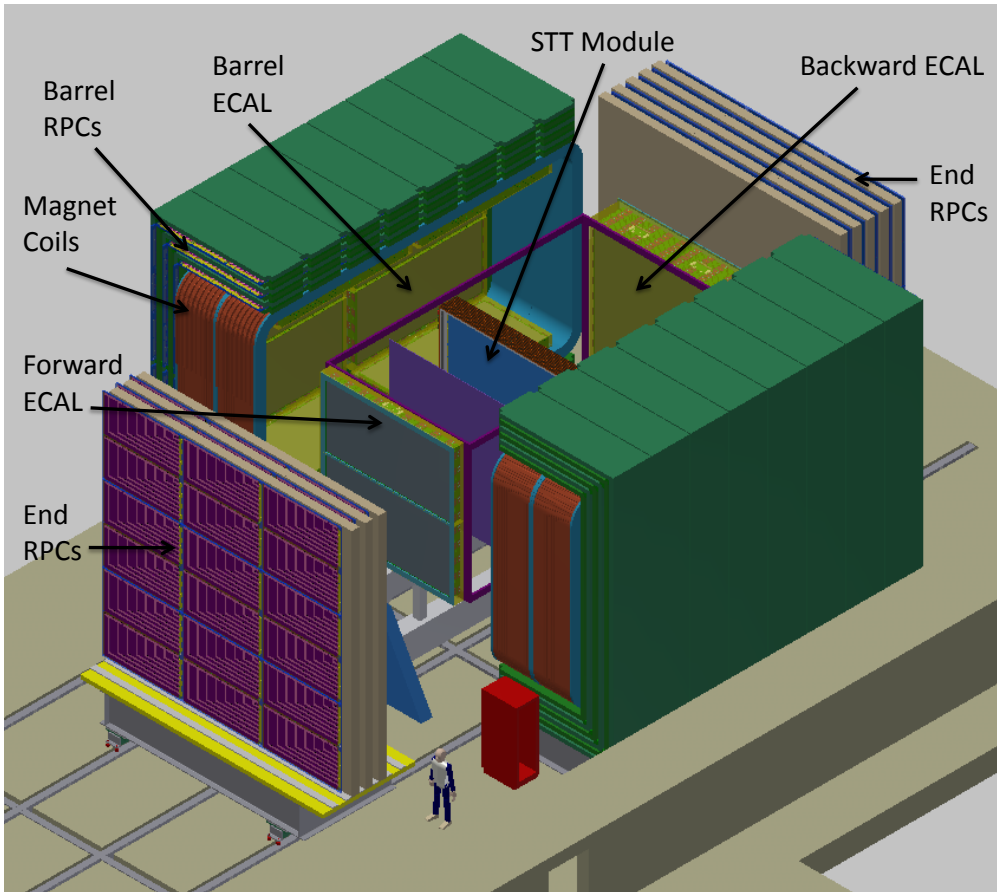

Figure 2.1: A schematic drawing of the fine-grained tracker design.

Table 2.1: A summary of the performance for the FGT configuration

Performance Metric	FGT
Straw Tube Detector Volume	3.5m x 3.5m x 6.4m
Straw Tube Detector Mass	8 t
Vertex Resolution	0.1 mm
Angular Resolution	2 mrad
E_e Resolution	5%
E_μ Resolution	5%
$\nu_\mu/\bar{\nu}_\mu$ ID	Yes
$\nu_e/\bar{\nu}_e$ ID	Yes
NCπ^0/CCe Rejection	0.1%
NCγ/CCe Rejection	0.2%
CCμ/CCe Rejection	0.01%

Table 2.2: Specifications for the FGT

Item	Requirement
Inner Magnetic Volume	4.5m x 4.5m x 8.0m
Tracking Detector	3.5m x 3.5m x 6.4m; 80 modules; 107,520 straws
Targets	1.27-cm thick argon, water, and other nuclear targets
Transition Radiation Radiators	3.6-cm thick radiators
ECAL	X_0 = 10 barrel, 10 backward, & 20 forward; 26,112 scintillator bars
Dipole Magnet	0.4T; 2.4 MW; 60 cm thick steel
Magnetic Field Uniformity	$< 2\%$ magnetic field variation over inner volume
MuID	432 RPC modules interspersed between 20-cm thick layers of steel

2.4 Straw-Tube Tracking Detector

2.4.1 Straw Tubes

The Straw-Tube Tracking Detector (STT) at the center of the FGT will be composed of straw tubes with an outer diameter of 1 cm, as well as radiators and targets that reside next to the straw tubes (see Figure 2.2). Vertical (YY) and horizontal (XX) planes of straws will be alternated and arranged in modules, with each module containing close-packed double straw layers of vertical and horizontal straws (XXYY). Figure 2.2 shows a schematic drawing of an STT module with four straw-tube planes and radiators. An alternative design has also been considered; it calls for two planes of straws per module, XX, YY, and so on. It will have approximately the same number of total straw tubes in the tracker but twice as many modules.

The performance and the cost of the STT are expected to be similar in both the reference (4-Planes/Module) and alternative (2-Planes/Module) designs. The straw tubes will be filled with a gas mixture of either 70% Ar plus 30% CO_2 (for modules with targets) or 70% Xe plus 30% CO_2 (for modules with radiators). The dimensions of each module in the reference design will be approximately 350 cm $\times$ 350 cm $\times$ 8.0 cm, including target or radiator planes and four straw planes. For ease of construction and transportation, each module is made up of six sub-modules, with dimensions of appproximately 350 cm $\times$ 117 cm $\times$ 2.0 cm. The straw tubes in a single sub-module will be able to provide the tension for the wires, however, a temporary sub-module carbon composite frame will be employed for shipping. The sub-modules will be assembled into modules at Fermilab, where each module will have a new carbon composite frame around the perimeter of the module for support and will have an attached target or radiator. Nominally, there will be 34 modules with targets and 46 modules with radiators, still keeping the average density of the STT at around 0.1 g/cm^3.

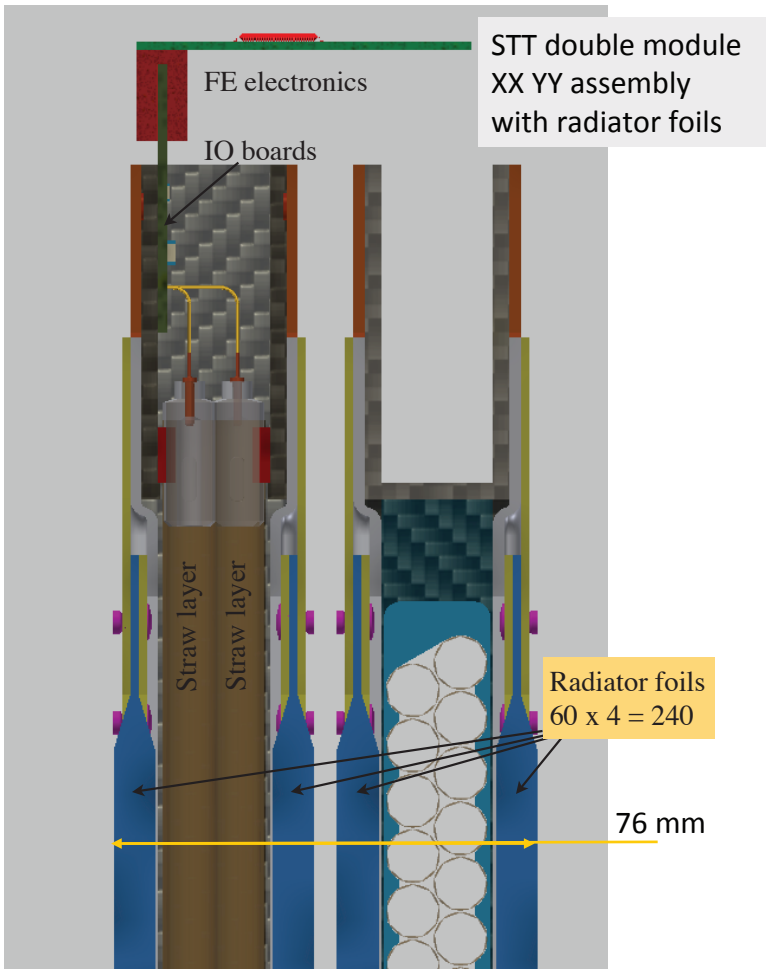

Figure 2.2: A schematic drawing of a STT module with four straw-tube planes and radiators (dark blue shading).

The STT will have a total of 107,520 straws — corresponding to 336 straws per plane, 1344 straws per module — and 80 modules. Both ends of the straw tubes will be read out, leading to a total number of electronics channels of 215,040. The total mass of the STT, including targets and radiators, is approximately 8 t, corresponding to an average density of 0.1. The thickness of the entire 6.4-m-long STT is almost two radiation lengths. Specifications for the Straw Tube Detector are shown in Table 2.3.

Table 2.3: Straw Tube Detector specifications

Item	Specification
Straw Tube Geometry	1cm Diameter x 3.5m Long
Number of Straw Tubes	107,520
Number of Straw Tubes per Plane	336
Number of Straw Tube Planes per Module	4
Number of Straw Tube Sub-Modules per Module	6
Number of Straw Tube Modules	80
Number of Straw Tube Sub-Modules	480
Length of Straw Tube Wire	376.3 km
Number of Electronics Channels	215,040
Number of Modules with Radiators	46
Radiator Thickness per Module	3.6cm
Radiator Mass per Module	108 kg
Number of Modules with Target Planes	34
Target Geometry	1.27cm Diameter $\times$ 3.5m long
Number of Targets per Plane	275
Ar Mass per Target Plane	15.5 kg
Water Mass per Target Plane	95 kg

2.4.2 Radiator Targets

Radiators will be placed in the downstream STT modules and will serve as targets for both neutrino interactions and Transition Radiation (TR) production. Each STT module contains four radiators, where each radiator consists of 60 layers of 25-μm polypropylene $(C_3H_6)_n$ foils alternating with 60 sheets of 125-μm tulle fabric spacers. The mass of each radiator is $\sim$ 27 kg and the thickness is $\sim$ 9 mm. Thin graphite planes and/or carbon fiber foils can be added to some STT modules in order to have a total carbon target mass of about 0.5 t. (This is in addition to the carbon in the STT frames.) A statistical subtraction of events occurring on the pure carbon target from the ones in the polypropylene radiators will provide a measurement of antineutrino interactions on a free proton target, which can be used for flux determination and cross section measurements.

2.4.3 Argon, Water, and Other Nuclear Targets

Both argon and water will be implemented as target materials for neutrino interactions. The argon targets will measure neutrino interactions on the same material as the far detector, while H_2O and D_2O water targets can be used to determine, through subtraction, the neutrino fluxes off of "free" neutron targets. Antineutrino fluxes off of "free" proton targets can be obtained, through subtraction, from C and CH_2 targets. The targets will be positioned directly upstream of individual modules without radiators. The targets, shown in Figure 2.3, will consist of planes of 0.5-inch diameter, 3.5-m-long aluminum tubes filled either with water (H_2O or D_2O) or with argon gas pressurized to 140 atm ($\rho = 0.233$). We will place 273 tubes in each plane, spaced 0.505-in apart. The tube wall thickness will depend on the fill material. Additional nuclear targets, such as Ca (same atomic weight as argon), C, stainless steel, and Pb, can also be used in the form of thin planes, to be positioned directly upstream of individual STT modules without radiators.

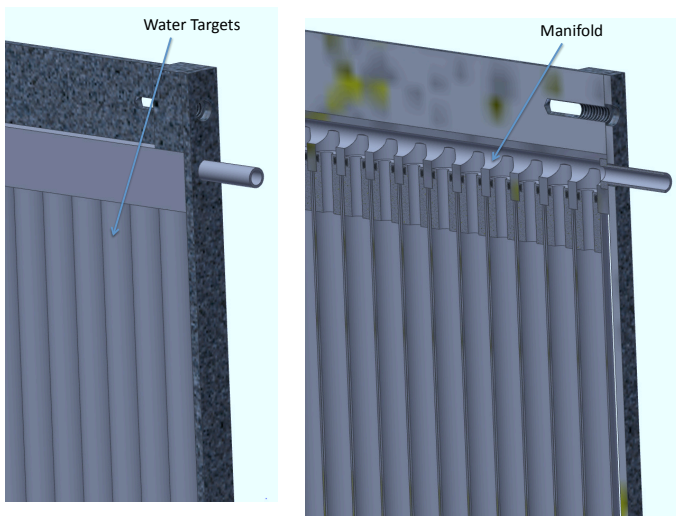

Figure 2.3: Schematic drawing of the water or pressurized-argon targets, made from 0.5-in diameter aluminum tubes.

2.5 Electromagnetic Calorimeter

An electromagnetic calorimeter (ECAL) will surround the tracking volume on all sides and consist of three separate pieces: Forward ECAL, Barrel ECAL, and Backward ECAL. The ECAL conceptual design consists of layers of either 1.75-mm-thick (for the forward ECAL) or 3.5-mm-thick (for the barrel and backward ECAL) lead sheets and 2.5-cm-wide by 10-mm-thick plastic scintillator bars, as shown in Figure 2.4. The scintillator layers for the Forward and Backward ECAL alternate as XYXXYXY..., while the scintillator layers for the Barrel ECAL are all horizontal along the axis of the magnet. The Forward ECAL will consist of 60 layers of scintillator bars, where each bar has dimensions 3.2 m $\times$ 2.5 cm $\times$ 1 cm. The Backward ECAL will consist of 16 layers of scintillator bars, where each bar has the same dimensions, 3.2 m $\times$ 2.5 cm $\times$ 1 cm. The Barrel ECAL will also

consist of 16 layers of scintillator bars, where each bar has the same dimensions, 3.2 m × 2.5 cm × 1 cm.

The lead sheets and scintillator bars will be assembled and glued together into complete modules of dimension 3.2 m × 3.2 cm × 81 cm for the Forward ECAL and 3.2 m × 3.2 cm × 27.5 cm for the Backward ECAL. For the Barrel ECAL, the module dimensions will also be 3.2 m × 3.2 cm × 27.5 cm. Two Barrel modules are placed end-to-end along the sides of the inner surface of the magnet (eight Barrel modules total) to provide full coverage of the barrel region. The total numbers of scintillator bars in the Forward, Backward, and Barrel ECAL are 7,680, 2,048, and 16,384, respectively, for a total of 26,112 bars.

The scintillator bars will be extruded with holes in the middle of each bar. The holes will then be fitted with 0.7-mm-diameter Kuraray wavelength-shifting (WLS) fibers. The fibers will be read out by SiPM (silicon photomultiplier) photosensors at each end, making the number of readout channels twice the number of scintillator bars for a total of 52,224. The total mass of scintillator is 20.9 t, the total mass of Pb is 70.8 t, and the total length of fiber is 83.6 km. Specifications for the ECAL are shown in Table 2.4. Figure 2.5 shows a side view of the ECAL (red) inside the dipole magnet, where there is very little gap between the Barrel ECAL and the Forward ECAL.

Table 2.4: ECAL specifications

Item	Specification
Scintillator Bar Geometry	3.2m × 2.5cm × 1cm
Number of Forward ECAL Scintillator Bars	7680
Forward ECAL Pb thickness	1.75mm
Number of Forward ECAL Layers	60
Number of Forward ECAL Radiation Lengths	20
Dimensions of Forward ECAL Module	3.2m × 3.2m × 81cm
Number of Barrel ECAL Scintillator Bars	16,384
Barrel ECAL Pb thickness	3.5mm
Number of Barrel ECAL Layers	16
Number of Barrel ECAL Radiation Lengths	10
Number of Barrel ECAL Modules	8
Dimensions of Barrel ECAL Modules	3.2m × 3.2m × 27.5cm
Number of Backward ECAL Scintillator Bars	2048
Backward ECAL Pb thickness	3.5mm
Number of Backward ECAL Layers	16
Number of Backward ECAL Radiation Lengths	10
Dimensions of Backward ECAL Module	3.2m × 3.2m × 27.5cm
Total Length of 0.7mm Diameter WLS Fiber	83.6km
Total Number of Scintillator Bars	26,112
Total Number of Electronics Channels	52,224
Total Mass of Scintillator	20,890 kg
Total Mass of Pb	70,800kg

Figure 2.4: Schematic drawing of the ECAL, which is made up of alternating planes of plastic scintillator and Pb sheets.

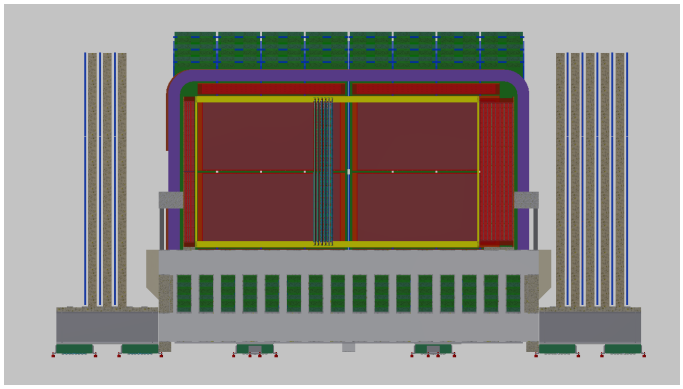

Figure 2.5: A side view of the ECAL (red) inside the dipole magnet, where there is very little gap between the Barrel ECAL and the Forward ECAL.

2.6 Dipole Magnet

The STT and ECAL modules will reside inside a 0.4-T dipole magnet for the measurement of particle momentum and charge. The magnet will have inner dimensions (inside the coils) 4.5-m wide × 4.5-m high × 8.0-m long. The magnet has four vertical Al coils, stacked horizontally, producing a horizontal magnetic field. The return yoke will be divided into two halves along the longitudinal center line to allow the magnet to be opened to service the detector inside, as shown in Figure 2.1. Each half yoke will be built from eight "C" (C-shaped) sections, and the thickness of the magnet steel will be 60 cm, consisting of 6 × 10-cm-thick plates. The magnet power requirement with Al coils is ∼ 2.4 MW, corresponding to 6 kA at 400 V. The water flow required for cooling is 20 l/s. The Dipole Magnet specifications are shown in Table 2.5.

The momentum resolution is dominated by multiple scattering in the STT. The momentum resolution is, therefore, given by $\delta p/p = 0.053/\sqrt{(LX_0)}B$. For B = 0.4T, L = 3m, and X_0 = 4m, the expected momentum resolution is ∼ 3.8%.

2.7 Muon Identifier

The sides and ends of the dipole magnet will be instrumented with a muon identifier detector (MuID) that will distinguish muons from hadrons by the ability of muons to penetrate the iron without showering or interacting. The MuID will consist of 432 resistive plate chamber (RPC) modules interspersed between two 10-cm-thick steel plates of the dipole magnet and between 20-cm-thick steel plates at the upstream and downstream ends of the magnet. The MuID is only meant to provide identification of the muon; the muon momentum will be measured by the STT

Table 2.5: Dipole Magnet specifications

Item	Specification
Inner Dimensions	4.5m x 4.5m x 8.0m
Magnetic Field	0.4 T
Number of "C" Sections	16
Thickness of Steel in the "C" Sections	60cm
Mass per "C" Section	60 t
Number of Coils	4
Mass per Coil	40 t
Magnet Current	6 kA
Magnet Voltage	400 V
Magnet Power Requirements	2.4 MW
Water Flow for Cooling	20 l/s

inside the magnetic field. A schematic drawing of the MuID interspersed in the magnet steel is shown in Figure 2.6.

The nominal dimensions of all RPC modules will be 1 m $\times$ 2 m with active areas of 96 cm $\times$ 196 cm. Each module has 256 X strips at 7.65-mm pitch and 128 Y strips at 7.5-mm pitch. The modules will be grouped into trays, each containing six modules, and the trays will be sufficiently wide to allow overlapping modules. The end RPC trays have dimensions of 2 m $\times$ 6 m, and there are three trays per plane. The downstream end has five planes, corresponding to 15 trays and 90 RPC modules. The upstream end has three planes, corresponding to nine trays and 54 RPC modules. The vertical barrel-RPC trays have dimensions of 2.5 m $\times$ 4 m, 2.8 m $\times$ 4 m, and 3.1 m $\times$ 4 m for the inner, middle, and, outer planes, respectively, corresponding to 24 trays and 144 RPC modules. The horizontal barrel-RPC trays have dimensions of 2.2 m $\times$ 4 m, 2.5 m $\times$ 4 m, and 2.8 m $\times$ 4 m for the inner, middle and outer planes, respectively, corresponding to 24 trays and 144 RPC modules. Overall, there are a total of 72 trays, 432 RPC modules, and 165,888 strips and electronic channels.

The downstream MuID will contain five steel planes of overall dimensions $6 \times 6 \times 0.2$ m^3 (283.5 t) and five RPC planes, while the upstream MuID will contain three steel planes (170.1 t) of dimensions $6 \times 6 \times 0.2$ m^3 and three RPC planes. The barrel MuID will contain 24 planes (three layers $\times$ eight sides) of RPCs. The RPCs will have a total thickness of 15 mm and a gap width of 2 mm. One possible gas mixture could be of Ar (75%), tetraflouroethane (20%), isobutane (4%), and sulphurhexaflouride (1%). Figure 2.7 shows a schematic drawing of an end RPC tray, while Figure 2.8 shows a schematic drawing of an RPC module. MuID specifications are shown in Table 2.6.

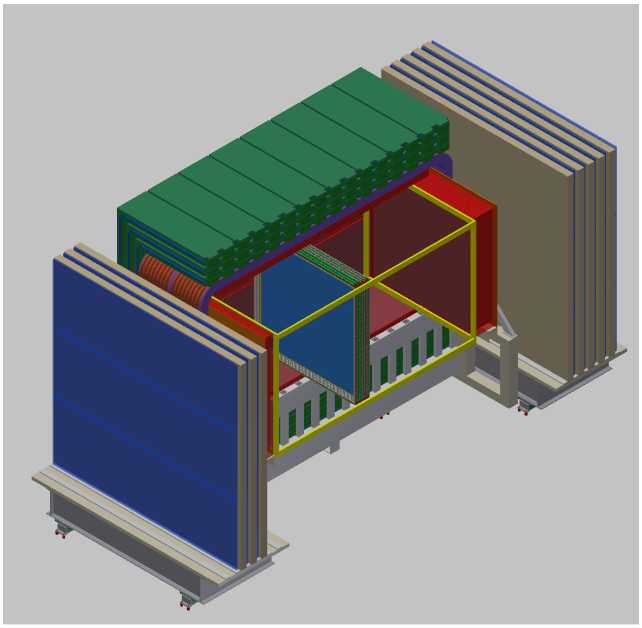

Figure 2.6: Schematic drawing of a magnet half-assembly, showing the the MuID interspersed in the magnet steel.

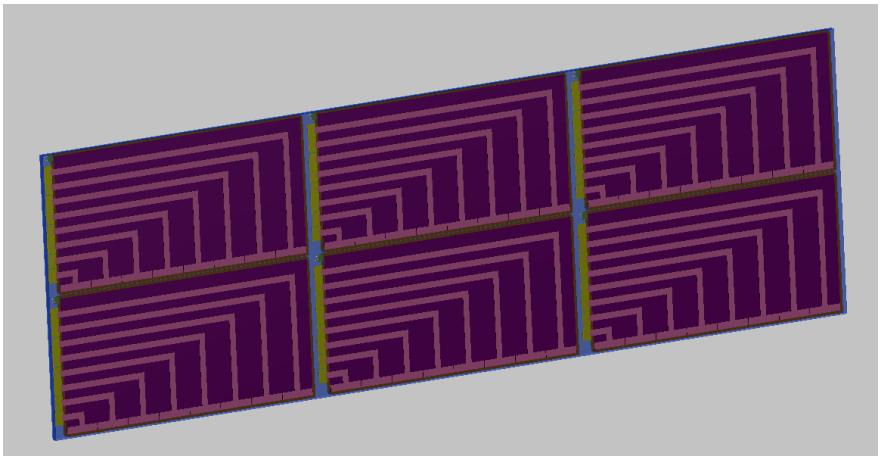

Figure 2.7: Schematic drawing of an end-RPC tray, consisting of six RPC modules of dimension 1m $\times$ 2m.

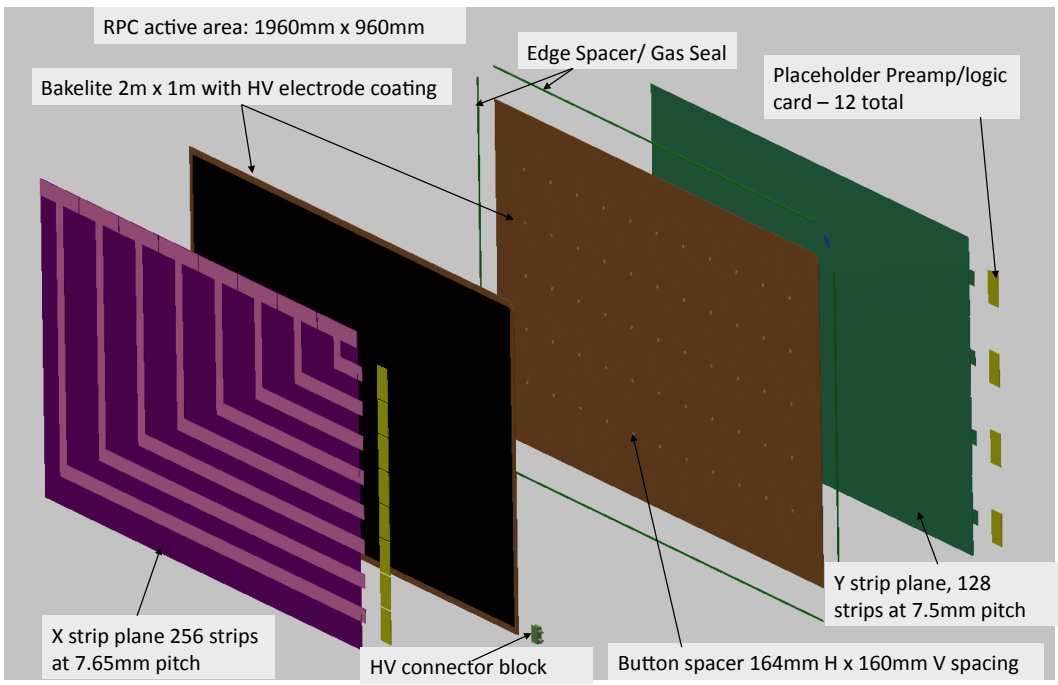

Figure 2.8: Schematic drawing of an RPC.

Table 2.6: MuID specifications

Item	Specification
Number of Barrel RPC Trays of Dimension 2.2m × 4m	8
Number of Barrel RPC Trays of Dimension 2.5m × 4m	16
Number of Barrel RPC Trays of Dimension 2.8m × 4m	16
Number of Barrel RPC Trays of Dimension 3.1m × 4m	8
Number of END RPC Trays of Dimension 2m × 6m	24
Total Number of RPC Trays	72
Total Number of RPC Modules	432
Mass of Downstream Steel Planes	283,500 kg
Mass of Upstream Steel Planes	170,100 kg
RPC Thickness	1.5cm
Number of 7.65mm Pitch X Strips per Module	256
Number of 7.5mm Pitch Y Strips per Module	128
Total Number of RPC Strips and Electronics	165,888

2.8 FGT Instrumentation

The instrumentation includes both fast readout electronics for the subdetectors and the slow control ($\mathcal{O}$ seconds) of the subdetectors, involving monitoring the humidity, temperature, gas pressure, etc. There is considerable synergy in the information gathered in the STT, ECAL and MuID. Both the STT and ECAL are required to measure the total charge and the time associated with a given hit. The MuID RPCs are required to provide the position and time associated with a traversing track. Similarly, the slow control of the subdetectors share many features. A brief description of the subdetector instrumentation is presented here, while Table 2.7 summarizes the number of electronics channels for each of the subdetectors.

Table 2.7: The number of electronics channels for each of the three detector systems

Detector	Number of Electronics Channels
STT	215,040
ECAL	52,224
MuID	165,888

2.8.1 Readout Electronics

The electronics for the three subsystems, STT, MuID, and ECAL, are all "fast" systems, i.e., all of the signals are in the few-to-10 nanosecond range. The STT output has a roughly 10-nanosecond rise time with a total integrated charge of about 100 electrons per centimeter. The gain of the STT drift tubes are typically 10^4 to 10^6, so over a collection time interval of $\sim$ 100 ns the integrated charge is 10^6 to 10^8 electrons. The MuID system contains RPCs that can operate in either streamer

mode or avalanche mode; the difference being that streamer mode is not proportional to the deposited charge, whereas the avalanche mode is. The rise time of the RPC signal is a few nanoseconds and charge is collected immediately; the collected charge can be large, up to 100 pC. The ECAL signals come from a SiPM that converts the light from the scintillator strips to an electronic signal. The deposited charge in the scintillator will give rise to 10^3 to 10^5 photoelectrons. The gain of a SiPM is $\sim 10^6$ and has a rise time of a few nanoseconds, so the total charge can be > 100 pC. As these three systems all have gain and are fast, it is hoped that a common electronics system may be possible.

The requirements for each system are very similar: a fast output and both an ADC and a TDC on each channel. Additionally, for the STT straw tubes it is desirable to wave-form digitize the analog signal in order to enhance the ability to separate the ionization signal from the transition radiation signal. The total channel count is 433,152 channels; this is broken out into 215,000 for the STT, 165,000 for the MuID, and 52,224 for the ECAL. Most available electronic systems from existing experiments don't quite meet these requirements or are too expensive to implement for this channel count ($50/channel has been allocated). Recently, an interesting new ASIC development for an upgrade to the ATLAS muon system at the LHC has come out of BNL (see talk given by Gianluigi De Geronimo at the ACES 2014 meeting at CERN in March 2014). A schematic of the newly developed chip (VMM2) is shown in Figure 2.9. It handles 64 channels and produces both fast ADC and TDC outputs. It has been fabricated and tested and should be ready by 2017, long before it will be needed for DUNE. The VMM2 features are the following:

- front-end electronics (ASIC)
- more than 2.3 million channels total
- operation with both charge polarities
- sensing element capacitance of 10-200 pF
- charge measurement up to 2 pC at < 1 fC RMS
- time measurement ~ 100 ns at < 1 ns RMS
- trigger primitives, neighbor logic
- low power, programmable

The VMM2 chip will be explored as the first option for the NND readout.

2.8.2 Humidity and Temperature Monitoring

Humidity is detrimental to all the FGT subdetectors. To maintain a low level of humidity and to maintain a desired temperature, both STT and ECAL subdetectors will have dry nitrogen circulating within their outer layers. A similar arrangement might be made for the RPCs, as

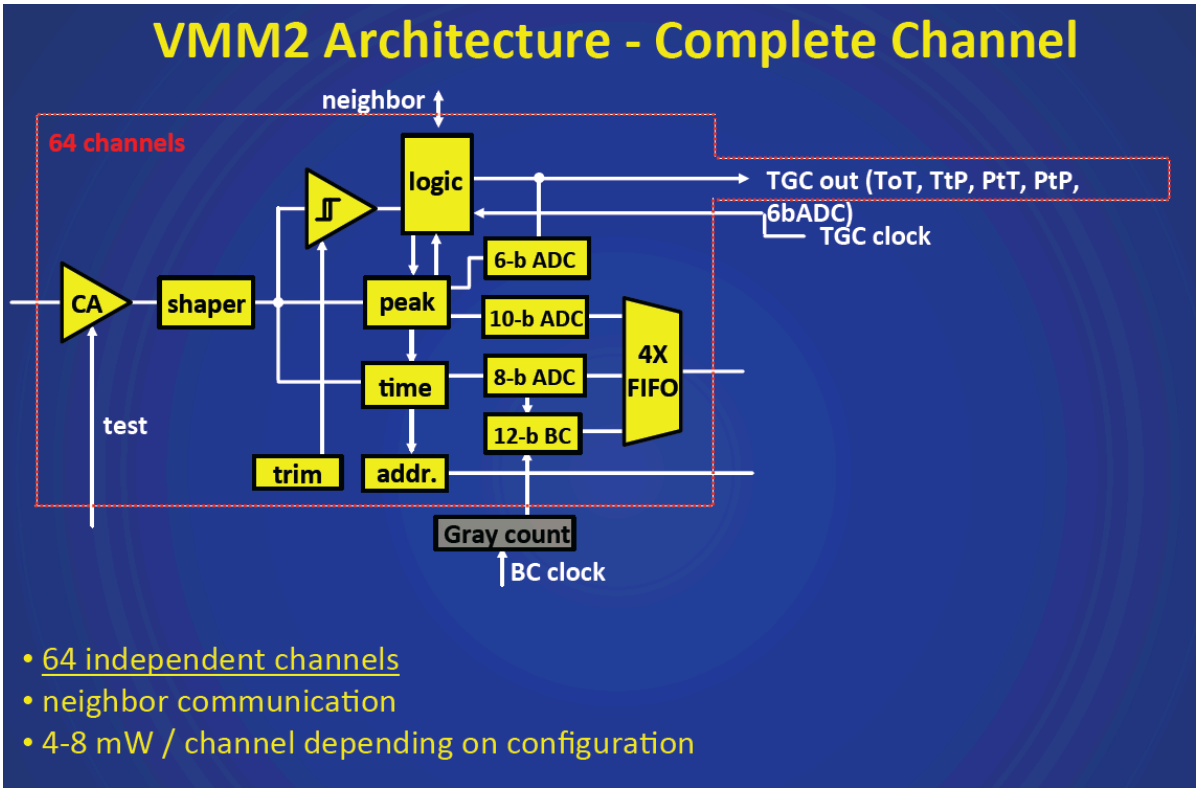

Figure 2.9: A schematic drawing of the VMM2 circuit.

well. Regarding the magnets, magnet coils are cooled by water, while the magnet yokes are instrumented with RPCs that must remain dry. Thus, a continuous control of humidity in all these detectors is needed. Just as for humidity, temperature must be continuously monitored in all of the subdetectors in order for the electronics to not overheat.

2.8.3 Gas Leak Monitoring in the STT and MuID

Gas leaks need to be monitored in the STT and MuID. The STT will employ Xe gas, which helps with the measurement of transition radiation. Xe gas is expensive and, hence, will be recirculated; leak-monitoring is particularly important here. The requirement on leaks is less stringent for the RPCs, which have less expensive gas.

2.8.4 Magnet Monitoring

The water flow (pressure gradient) will be continuously monitored in order to ensure that the magnet does not overheat. Also, all power sources instrumenting the FGT and its readout need to be monitored for appropriate voltage and current.

Chapter 3

Near Detector Beamline Measurements

3.1 Introduction

This chapter outlines the DUNE strategy for measurements of secondary beam particles in the region behind the beam absorber. Those measurements are designed to provide constraints on the neutrino flux at the near and far detectors, and data on the pulse-to-pulse variation of the beam for beam diagnostic purposes. A description of equipment for monitoring the proton beam's interaction with the proton target can be found in Volume 2: The Beamline at the Near Site.

The measurements and apparatus described in this chapter fall into the category of equipment designed specifically for DUNE to detect muons exiting the decay tunnel.

3.2 Design Considerations

3.2.1 General

The requirements for the beamline measurements, as discussed in the NDC requirements documentation [1], are intimately related to how well the neutrino flux must be known. Given that DUNE does not have the luxury to construct identical Near and Far Detectors, a near-far comparison is more complicated than it was in the MINOS experiment [2], for example. While external hadron-production measurements can place strong constraints on the pion and kaon production in the target, they do not provide any confirmation of the simulation of other key features, such as the horn focusing, secondary interactions, and the pion scattering and absorption in the air-filled decay volume.

In addition to the external measurements, covered in Section **??**, that confirm the simulation of the thick target, horn material, decay tunnel and absorber, it is desirable to constrain the flux by

making independent measurements at the 4–5% level of the muons that penetrate the absorber. It would not be practical to do this for all penetrating muons, but sufficient measurements at a few positions can be done in a cost-effective way.

3.2.2 Muon Measurements

The dominant, two-body decays of pions and kaons that produce neutrinos also result in the creation of daughter muons. Monitoring the muons exiting the decay volume can provide information about the direction, size, shape and flux of the neutrino beam. The daughter muon and neutrino energies in those two-body decays are completely anti-correlated. For example, a $\pi^+ \rightarrow \mu^+\nu_\mu$ decay will result in a ν_μ with an energy, E_ν, between zero and $0.43E_\pi$ plus a μ^+ with an energy of $E_\mu = E_\pi - E_\nu$ between $0.57E_\pi$ and E_π. This has the effect that the muon takes 79% of the pion energy on average, leaving the neutrino with only 21%. Thus, on average, the muon energy is 3.75 times that of the neutrino.

The primary physics goal of DUNE is to measure the transmutation of ν_μs to ν_es over the 1300km between Fermilab and the far detector site. Therefore it is essential for DUNE to cross-check the estimate of background ν_es present in the beam by using several methods to measure their rates at the Fermilab site. There are two dominant sources of ν_es present in the neutrino beam, muon decays and kaon decays. The muon systems are designed to directly measure the muons that penetrate absorber with an energy threshold as low as possible, i.e. directly measure those muons whose decays are a major source of background ν_es, . A measurement of the spectrum of those muons will translate directly into constraints on the spectrum of background ν_es. That constraint has the enormous advantage of being independent of poorly understood neutrino-nucleus cross sections.

Because muons and neutrinos come from the same parent pion and kaon decays, a measurement of the absolute muon flux in conjunction with the energy spectrum seen in the muon monitors can constrain the absolute neutrino flux. The goal for the DUNE muon monitors is to determine the absolute muon flux to an accuracy of 5% above a muon energy of 6 GeV (which corresponds to a neutrino energy of 1.6 GeV) in the central part of the absorber. Figure 3.1 shows the total simulated neutrino flux at the Far Detector overlaid with the flux from only neutrinos having pion or kaon parents that contribute to the signal seen in the muon monitor. The simulation shows that between 3 GeV and 10 GeV, more than 90% of the neutrinos in the Far Detector come from this subset.

It is essential to monitor the stability of the beam direction over time. Figure 3.2 shows the effect on the muon-neutrino flux in the Far Detectors when the beam is misaligned by 0.4 mrad. For example, above 6 GeV, the ratio of the Far Detector flux over the Near Detector flux changes by 2%. To keep the change in the neutrino beam less than 1% in all energy bins, the beam direction must be known to a precision of approximately 0.2 mrad. Because the muon monitors will be located approximately 275 m from the beam target, this requires a measurement of the muons to an accuracy of approximately 5 cm.

The rate of muons crossing the monitors will be quite high, with preliminary LBNF beam simula-

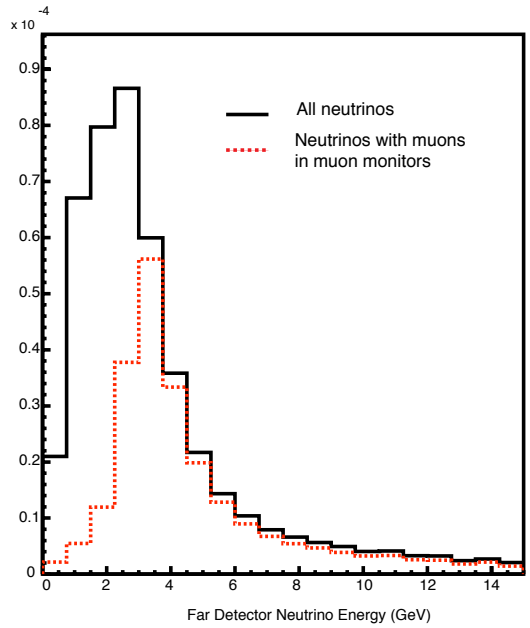

Figure 3.1: The total simulated neutrino flux at the Far Detector (black solid) overlaid with the neutrino flux, also at the Far Detector, coming from neutrinos with pion or kaon parents that contribute to the muon-monitor signal (red dashed), averaged over the back of the absorber. As shown in Figure 3.6, the muon systems will probe down to 1.5 GeV in neutrino energy on the beam axis.

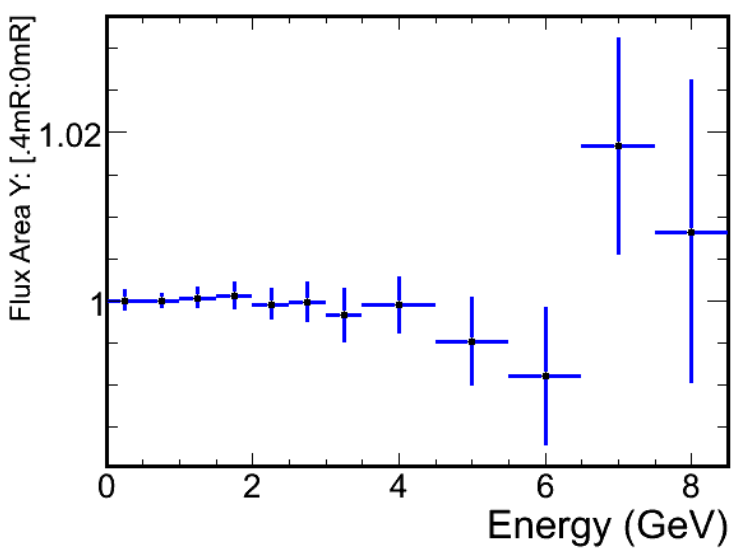

Figure 3.2: Ratio of the neutrino flux on-axis to the flux 0.4 mrad off-axis at the Far Detector position.

tions suggesting approximately 50 million muons per cm^2 for a pulse of 10^{14} protons-on-target. The muon monitors must also be capable of operating in a high-radiation environment. For example, the expected dose in the area downstream of the NuMI absorber is as high as 100 MRad per year [3].

3.3 Muon-Measurement Facilities

The muon measurements are carried out in the region immediately following the hadron absorber at the end of the decay tunnel, below the Absorber Service Building (LBNF 30). A view of the absorber area and the muon alcove is shown in Figure 3.3. The axis of the decay pipe cuts across the muon alcove at an angle, and the size of the alcove is largely determined by the requirement that it contain the shadow of the four-meter-diameter decay pipe, projected through the alcove, as shown in the elevation view of Figure 3.5.

Figure 3.4 shows the downstream side of the absorber and a conceptual layout of the muon systems described in various sections of this chapter. The absorber itself is encased in concrete. The first set of muon-measurement devices, from left to right, is a set of three variable-pressure gas Cherenkov counters, which are mounted directly to the rear wall of the absorber. Following that is an array of diamond ionization detectors and finally a set of stopped-muon counters which are interspersed between walls of steel "blue blocks". The blue blocks are there to provide several depths at which to monitor the stopped muons as they range out in the material. A second array of ionization devices will also be placed farther downstream within the blue blocks.

A perspective view of LBNF 30 is shown in Figure 3.4, and a detail of the lower level of Absorber Hall is given in Figure 3.5. The HV, water systems and gas systems for the muon monitors will be located nearby on the lower level. The readout electronics will be located in racks close to the surface.

It is important to have precise knowledge of the amount of material muons pass through before they are registered in the muon systems. The absorber itself is a complex, heterogeneous assembly of various materials. Figure 3.5 show the absorber conceptual design (more detail is available in Volume 2 of this CDR). A hole in the front side of the absorber, at left, is both surrounded and followed by the aluminum core of the absorber. The core is then surrounded by steel and standard steel "blue blocks", which are in turn surrounded by concrete. This complex geometry must be carefully understood and simulated in order to make the muon measurements effective.

Figure 3.6 shows the energy lost by a horizontal muon as it traverses the absorber, as a function of the distance from the beam axis along a 45° line perpendicular to the beam axis. In the central region, roughly to a distance of 105 cm, the muons lose between 5.0 to 6.4 GeV, so that the lowest-energy muons leaving the absorber at that point correspond to neutrino energies of ~ 1.5 to 2.0 GeV. At a radius of roughly 105 cm, the full thickness of steel causes the muons 10 GeV or more, corresponding to neutrino energies of ~ 2.6 GeV. From the perspective of the muon systems it will be desirable to lower these thresholds if possible. This might be accomplished by using more aluminum in the front part of the absorber or by judiciously locating detectors inside the absorber

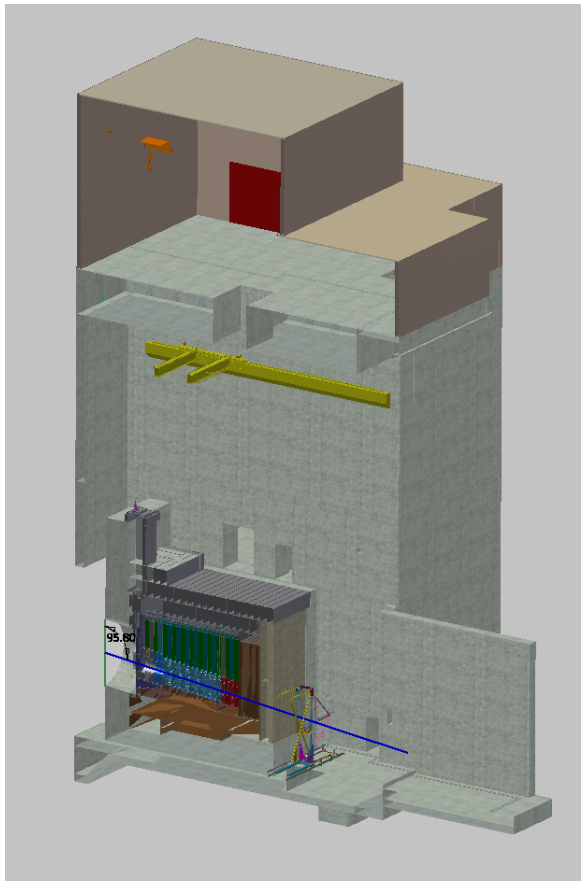

Figure 3.3: The Absorber Hall overview. The Absorber Service Building (LBNF 30) is on the surface and allows for crane access to the Absorber Hall. The muon alcove is directly behind the absorber.

Figure 3.4: A perspective view of the Absorber Hall area.

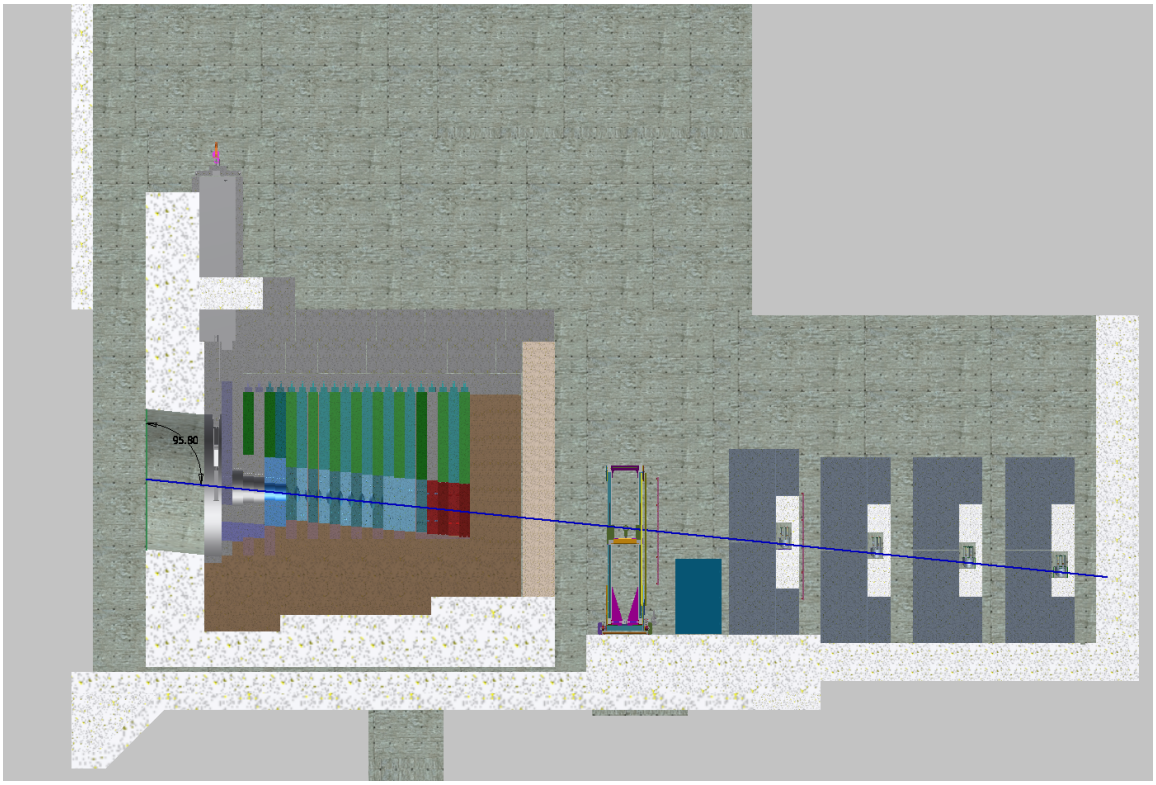

Figure 3.5: Absorber conceptual design. The figure shows the elevation view of the absorber at the end of the decay tunnel. The beam axis is shown by the blue line. The absorber is constructed of several different materials as shown: aluminum core in blue and grey, concrete (grey and tan), and steel (in brown and green).

material.

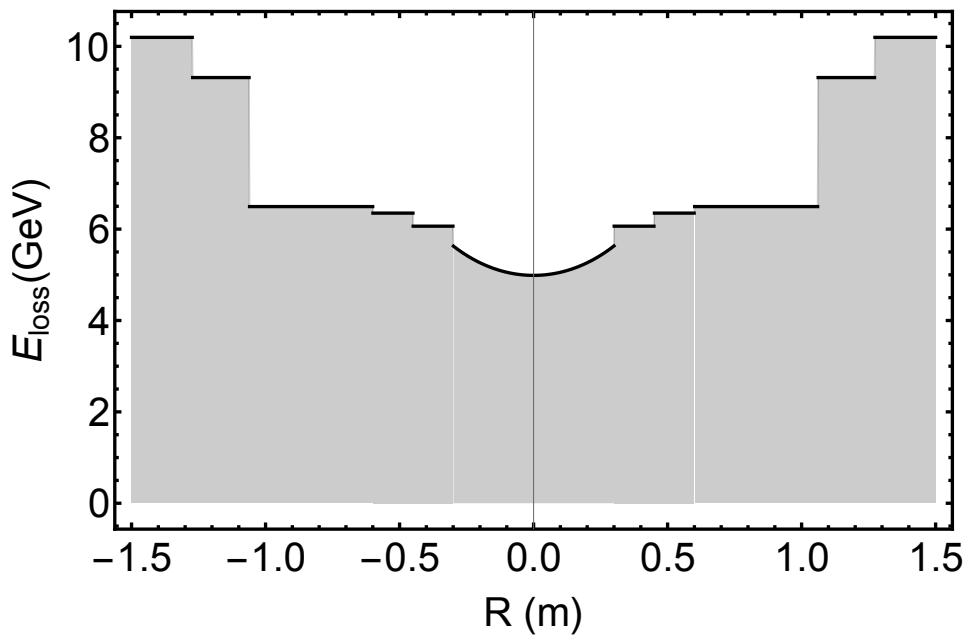

Figure 3.6: The energy loss a muon, parallel to the beam axis, experiences as it traverses the material in the absorber. The muon's energy loss is plotted versus the distance from the beam axis, along a 45 ° line perpendicular to the beam axis. Muons suffer between 4.7 and 9.3 GeV of energy loss depending upon where they cross the absorber.

3.4 Muon Cherenkov Detectors

3.4.1 Introduction

A Cherenkov variable-pressure, gas Cherenkov counter, operated in differential mode will be deployed downstream of the absorber. The counter will be mounted on a movable stand that will allow the system to scan in a plane transverse to the beam axis. The Cherenkov counter deployed by DUNE will not image individual Cherenkov rings, but rather will see the integrated signal from many muons due to the very large instantaneous flux. In addition, by varying the radiator gas pressure, and hence the Cherenkov threshold, the system's index of refraction will vary, allowing it to map out the muon momentum distribution.

Figure 3.7 shows the expected distribution of velocities, β (v/c), for muons and electrons after exiting the absorber. Figure 3.8 shows the expected angle with respect to the beam for electrons and muons with similar velocities (implying that both are visible above the same Cherenkov threshold). Despite the similar velocities, the muons are much more likely than the electrons to be directed parallel to the beam.

Therefore, a detector that takes advantage of the directional nature of Cherenkov light will have less background contributions from electrons and other isotropic background particles such as

neutrons, than will an ionization system, for example.

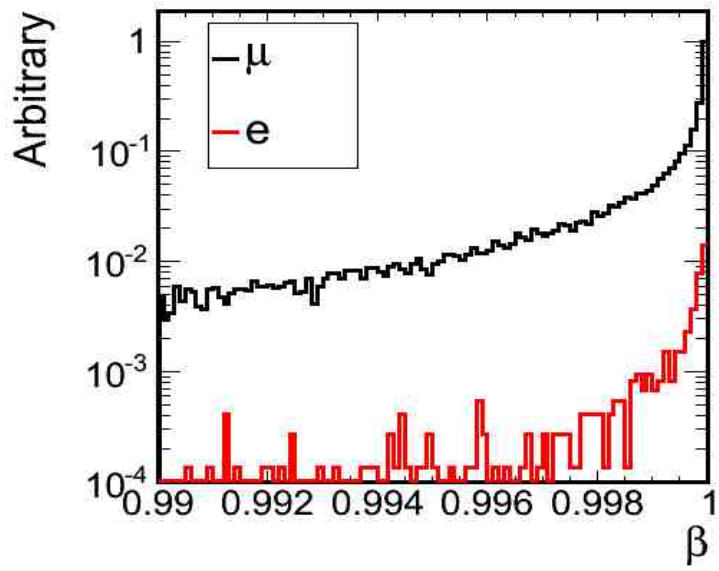

Figure 3.7: Simulated electron and muon velocities exiting the absorber. This plot is based on a simulation gnumi[4] of the LBNF beamline.

3.4.2 Reference Design

The simple Cherenkov counter design employs a gas radiator contained in a pressurized tube. The very forward Cherenkov light in a narrow cone of ± 1 mrad is collected at the end of the tube by a mirror that reflects the light 90 degrees towards a photosensor located outside the high-radiation field of the muon beam. The gas pressure, varied from vacuum to twenty atmospheres, will determine the index of refraction, and hence the Cherenkov angle versus muon-momentum. Several such tubes will be constructed in an array transverse to the beam direction. The resulting pressure scan will give the momentum distribution of the muons at an array of points across the end of the absorber.

Figure 3.9 shows how the Cherenkov system will be constructed. Safety considerations suggest that the diameter of the radiator tube and light-guide tube be six inches or less. A photosensor, located outside the direct radiation field of the muons, will view the primary mirror through a telescopic optical system.

The preferred option is to use a gas Cherenkov system containing a noble gas with a high index of refraction, where the density of the gas can be varied to change the Cherenkov threshold. The noble gas will reduce potential degradation due to reactivity in the high radiation field of the post-absorber environment. Varying the pressure will provide more information about the momentum spectrum of the muons.

The combination of a flat mirror and a 90^0 mirror will reflect light out to a PMT. The UV-sensitive PMT will collect light from normal incidence on the primary mirror with a 2 mrad acceptance, the

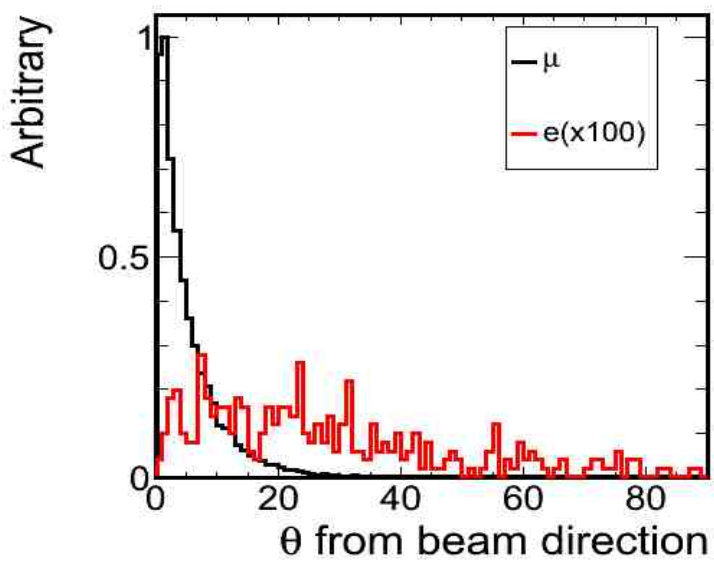

Figure 3.8: lSimulated plot of angle with respect to the beam for electrons and muons exiting the absorber. This plot is based on a gnumi simulation of the LBNF beamline.

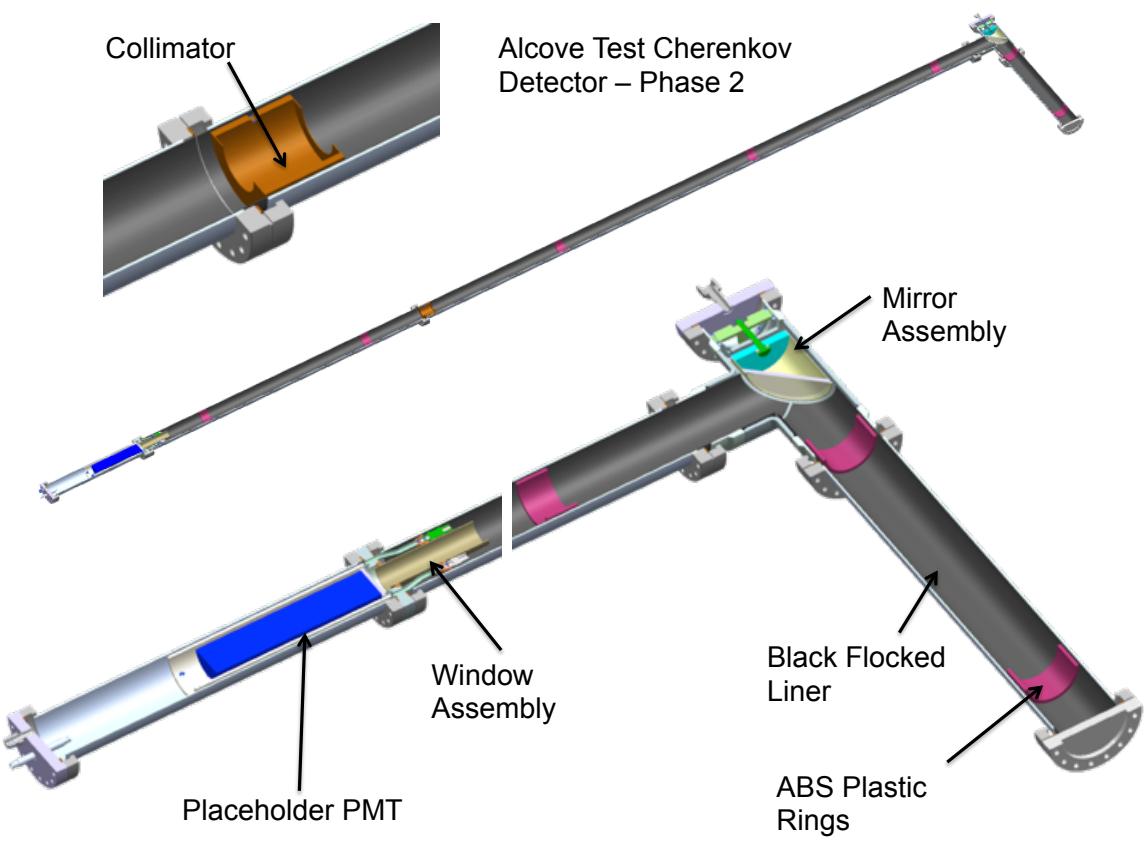

Figure 3.9: The Cherenkov counter prototype design. Muons at threshold momentum emit forward Cherenkov light which is reflected via one flat mirror 45 degrees) to a PMT located outside of the muon radiation field.

light yield per particle will be approximately one photon near threshold. That is more than ample light for the system where the particle flux is of order 10^7 per cm^2 through the radiator section.

3.4.3 Prototype Development and Testing

A prototype Cherenkov counter, along with associated fully automated gas systems, HV systems, and data acquisition system has been constructed and is undergoing testing in the NuMI neutrino beam's muon alcove 2. In addition, three diamond detectors [5] for ionization measurements have also been installed into the alcove. Figure 3.10 shows the prototype detectors in NuMI alcove 2.

The counter has an automated gas system with a settable pressure that ranges from vacuum to 20 atm, corresponding to muon Cherenkov thresholds of 200 GeV/c and 1 GeV/c respectively. When operated at vacuum, the PMT registers all background light unrelated to the gas, e.g. transition radiation, light from particles hitting the window and PMT glass. Those contributions are observed to be very small relative to the coherent, directional Cherenkov light.

The counter is constructed with a 1 meter long radiator section as shown in Figure 3.9 . A 20 foot extension allows the reflected Cherenkov light to travel to a sapphire pressure window viewed by a photo multiplier tube.

The prototype is now fully integrated into NuMI operations and real-time waveforms can be viewed online as shown in Figure 3.11. The top panel shows the waveform from the Cherenkov counter at 2 atm gas pressure, that corresponds to a muon momentum threshold of 3 GeV/c. The second panel shows the waveform from a $9mm \times 9mm$ diamond detector mounted to the front flange of the Cherenkov radiator section as shown in the inset of Figure 3.10.

The extracted NuMI proton beam, Resistive Wall Monitor (RWM) signal is also recorded with an identical digitizer. That allows a direct, bucket-by-bucket (individual proton pulses) comparison of the proton current onto the NuMI primary proton target, and the muons measured after the absorber with a 400ps time resolution.

A second set of muon detectors, the final DUNE design, are being constructed at this time (2015). They are being installed directly behind the NuMI proton beam dump (muon alcove 1). They will be mounted on a movable stand, and the entire setup will be eventually transferred the DUNE absorber hall. The higher radiation environment of alcove 1 will be more similar to the eventual DUNE installation. It will allow the DUNE muon detectors to be calibrated in the NuMI beam and ready for use in the DUNE beam.

3.4.4 Installation

Installation will begin following the absorber installation and the installation of the stopped muon systems systems. The counters will be removed from the NuMI Alcove 1 area after calibration in the NuMI beam, and then stored until they are needed for DUNE. The gas handling system will

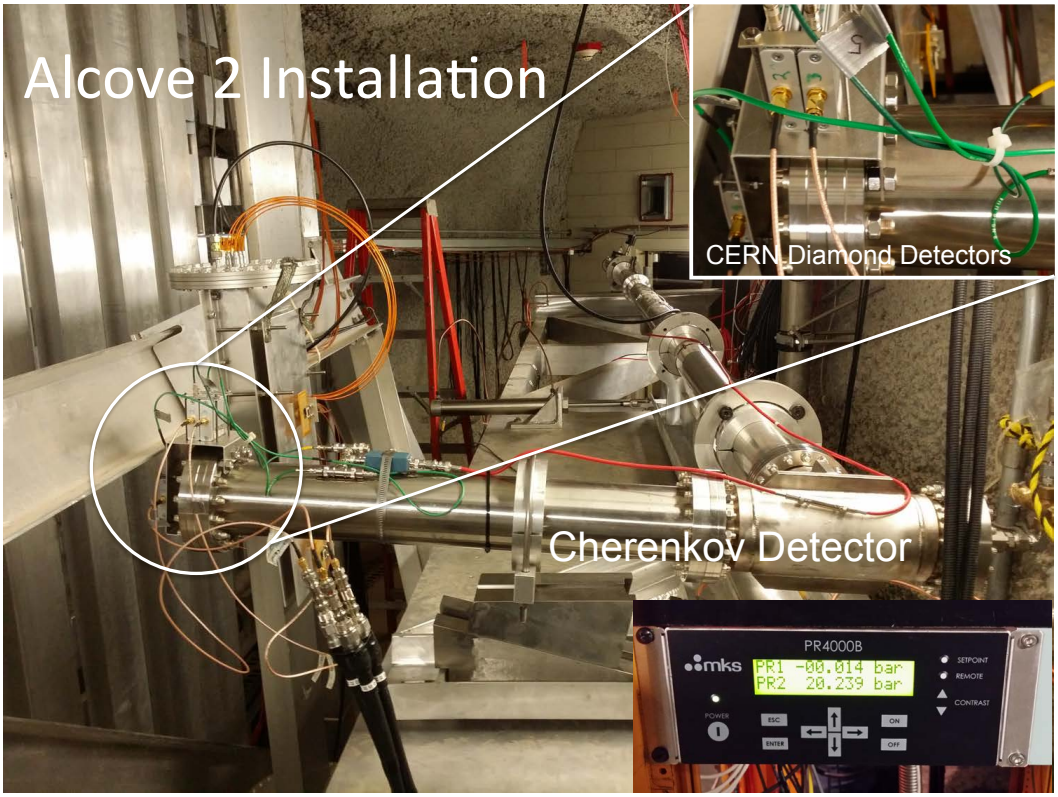

Figure 3.10: A prototype muon gas Cherenkov detector for DUNE. Muons travel through an L-shaped 4" Conflat pipe filled with a pressurized gas. A flat mirror mirrors directs the optical photons to a photo multiplier. The lower right inset shows the 20 bar MKS pressure reading achieved by the Cherenkov gas system, and the inset on the upper right shows the CERN/Cividec diamond detectors mounted to the Cherenkov housing.

Figure 3.11: The realtime display of the muon detector prototypes in operation on the NuMI beam line. The top two panels are the Cherenkov counter and CERN diamond detector [5], The signals are transmitted through low-loss heliax cable, and then the waveform is digitized at 2.5 GHz with a 12 bit dynamic range, and the recorded onto disk storage for analysis. The signal from the muons is contained in the short beam pulse "buckets" created by the accelerator RF structure. The fast timing allows the prompt muon signal to be easily separated from potential backgrounds such as stopped muon decays, beta decays, and neutrons.

be located nearby, also on the lower level of the Absorber Hall.

3.4.5 Operation

Because the system will be located in a radiation-controlled environment that will not be accessible during beam operation, it is essential that the electronics and gas handling system be both robust and remotely operable. The prototype system in use at the NuMI area can be relocated for that purpose, or if desired a new system may be constructed. Periodic access will be required to the utilities area to replace gas bottles.

3.5 Muon-Ionization Measurements

3.5.1 Introduction

Post-absorber muon measurements in most of the recent neutrino-beam experiments have typically employed a planar array of ionization counters to measure the muon profile and intensity. The NuMI beamline [3] and the K2K [6] [7] and T2K [8] [9] experiments have all utilized parallel-plate ionization detectors. These counters have been shown to work in the high-radiation environment.

K2K and T2K have also deployed solid-state silicon detectors [7] [10]. The advantage of silicon is that it is less sensitive to changes in the air temperature and pressure. However, these sensors are not as radiation-tolerant as the parallel-plate ionization chambers and will only be used in T2K for the initial beam operation.

DUNE is however in the process of evaluating CVD diamond detectors as ionization measurement devices. Their advantage is two-fold, they are much more radiation resistant than silicon, and they provide a much faster signal than ion chambers which allows them to distinguish between background and the prompt muon signal. They are also very stable and require no gas system.

The DUNE NDC plans to use the ionization devices, e.g. CVD diamond, to monitor the beam stability, direction and shape, and also potentially to determine the absolute flux of muons or to determine the muon-energy spectrum. Instead, the stopped-muon counters and gas Cherenkov detector will be used, respectively, to determine the flux and energy spectrum of the muons.

3.5.2 Reference Design

The reference conceptual design is to use CVD diamond ionization detectors arranged in two arrays. Each array will measure the centroid of the muon beam to insure a stable neutrino flux at

the near and far detectors. The detectors are arranged in a diamond shaped arrays as shown in Figure 3.4 and Figure 3.12.

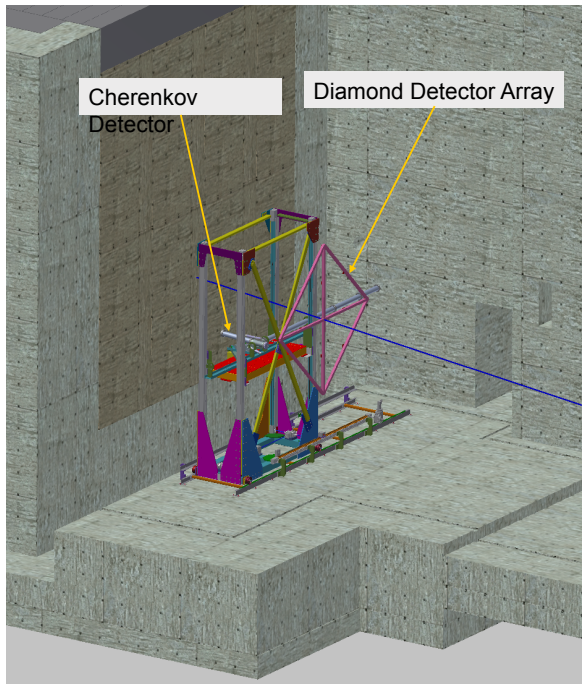

Figure 3.12: A model of the ionization detector layout behind the Cherenkov detector stand showing the 13 detectors in a grid configuration.

The reference design for DUNE includes two layers of ionization counters, one behind the absorber and a second one behind steel shielding blocks. DUNE wants to achieve a precision in the beam center of 0.2 milliradians (5 cm for a 250 m decay pipe). A quick study has determined the sensitivity for various arrangements of the ionization counters for each layer and Figure 3.14 shows the typical precision such a system can achieve. DUNE design was motivated by a desire to use a grid array with some of the counters removed, and still achieve the desired sensitivity, thus reducing the total number of needed counters.

Several different designs for the counter arrangement were studied and the area covered by the detectors was varied. A toy Monte Carlo model was developed to estimate the precision of each design. The muon profile was assumed to be a Gaussian with a spread of 130 cm in the x and y dimensions and a center at the origin. The standard deviation on the beam center was studied as a function of array coverage for several designs and for 2%, 5% and 10% random systematic error offsets. Figure 3.14 shows the precision of the detector array as a function of the width of the detector cross arrangement of the detectors.

The results show that the width of the detector array affects the precision more than the layout of the detectors. Increasing the array size improves the precision greatly.

The DUNE muon ionization detector design consists of two arrays of ionization counters, which is motivated by the NuMI target experience. Over a period of several months, the number of events per proton on target gradually decreased over time, especially in the energy range from 2-4 GeV. This reduction in neutrino flux is attributed to target radiation damage. Figure **??** shows the ratio

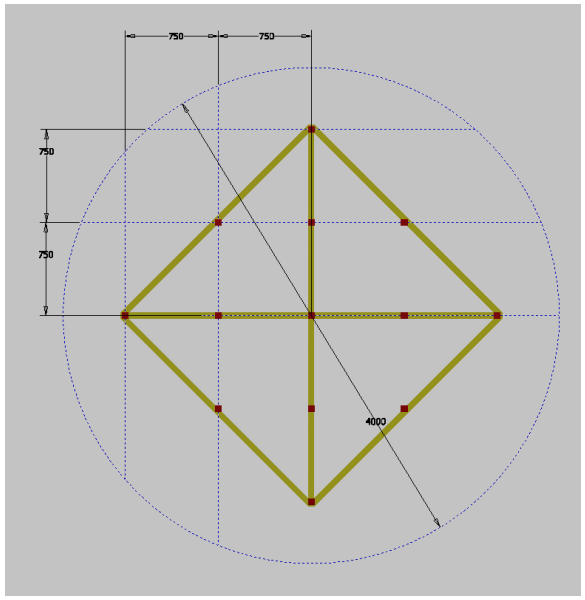

Figure 3.13: A model of one the two ionization detector arrays that measure the muon flux and muon beam centroid.

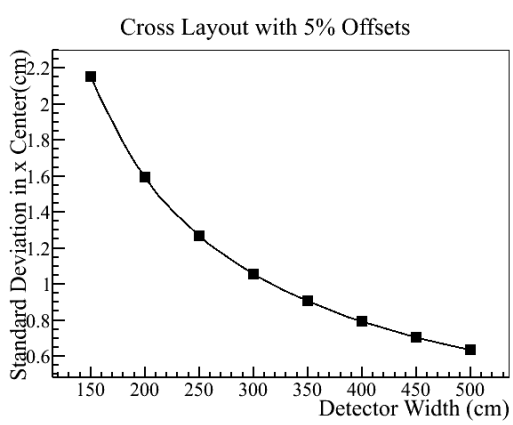

Figure 3.14: Precision as a function of detector width for a cross-shaped detector with assumed 5% random calibration offsets.

of the signal seen in the first muon alcove to the signal seen in the second muon alcove versus time. This ratio decreased in a similar manner over time. The first alcove was immediately after the absorber, while the second alcove was behind approximately 12 m of rock, and therefore saw only higher energy muons, since the lower energy ones would range out before reaching the second alcove. This gradual decrease in the ratio of the signals seen in these arrays was an indication of the target degradation and the relative reduction in the low-energy part of the neutrino and muon fluxes. [1]

It will be necessary to be able to monitor this ratio in DUNE on a spill-by-spill basis to look for signs of target degradation or horn failure. Therefore, a second ionization array, placed behind several layers of shielding blocks, will be necessary. In Figure 3.4 the second array is placed behind 4 m of steel shielding. Since the density of steel is roughly 3 times larger than that of rock, this is comparable to the depth of the NuMI second muon alcove, which sits behind 12 m of rock. More detailed studies will need to be performed to determine if this is the optimal location for sensitivity to changes in the target density.

3.5.3 Prototype Design and Testing

The prototype testing of the diamond detectors is described above in the Cherenkov counter section, Section 3.4.3. For the DUNE ionization detectors, a small array of prototype counters will be built and operated in the existing NuMI alcove 1 to determine the optimal design and operating conditions for the DUNE monitors. This will be done in 2016 and 2017. It will provide a good field test in roughly the same environment as expected during DUNE operations. It will also be cross-checked against the existing NuMI muon-monitoring system. The goals of these tests are to understand the linearity of the response of these counters (by comparing the observed signal to variations in the beam intensity), their long-term stability and operational reliability.

3.5.4 Installation

The system installation will begin following completion of the Absorber Hall and LBNF 30 and the installation of the stopped-muon counter system (described in Section 3.6).

3.5.5 Operation

The muon-monitor-system data will be displayed in the control room at the Absorber Hall upper level on a spill-by-spill basis to monitor the beam stability and look for potential signs of target or horn degradation. This control room will be accessible during the beam operation. The data will also be displayed at central run control.

[1] Similar trends were seen in the ratios of the other muon alcove signals, but the first/second ratio saw the largest effect.

3.6 Stopped-Muon Detector

3.6.1 Introduction

The second system under development is stopped-muon counters, also called Michel-electron detectors. This method will measure the muon flux without suffering from some of the disadvantages intrinsic to systems that detect through-going muons. The strategy employed here is to stop muons in a material with significant carbon content and, via muon capture, to produce ^{12}B that will in turn undergo β decay. The high-carbon material, in this case graphite, surrounds a Cherenkov radiator material which is sensitive to electrons from muon decay or high-energy beta decays. Figure 3.15 shows the conceptual design of a single stopped-muon counter.

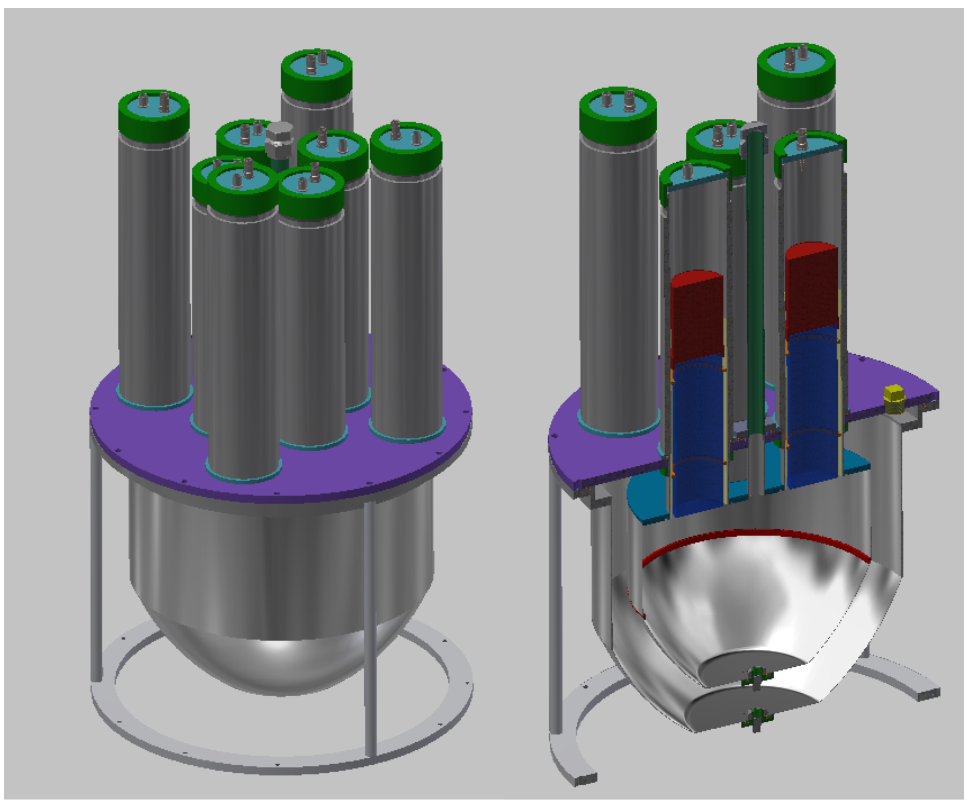

Figure 3.15: Conceptual design of a single Michel-electron detector (stopped-muon counter)

The detectors will only operate in the lower-rate environment that is present many microseconds after the beam pulse is over. There are two possible modes for this type of system. The first is an integrating mode where the characteristic decay time of 2.2 μs for muon decay and corresponding beta-decay lifetimes is used to unfold the total number of decays. The other mode under investigation uses the ability to record individual decays rather than an analog current measurement. This mode may allow a more precise absolute normalization of the flux and fit the muon lifetime in the Michel-electron detector. This will provide a more robust cross-check on the muon signal than will ionization detectors, which are sensitive to delta rays, photon conversions and other charged particles.

Although this technique has never been tried on a large scale, a small demonstration project in K2K was able to see Michel decays with a 10^3 signal/background ratio and to measure the absolute rate with 30% precision[11].

3.6.2 Reference Design

The stopped-muon detector reference design is modular and based on a Cherenkov radiator of minimum size to contain a 52.8-MeV electron and distinguish it cleanly from lower-energy radioactivity. This conceptual design employs a liquid mineral oil radiator. The radiator will be coupled to four photomultiplier tubes (PMT) or other photon counter. The entire module will be surrounded by a liquid scintillator veto layer, and the entire module then encased in a material that provides both a uniform-density stopping target for muons and some shielding from incoming neutrons. One or two signal channels will be associated with each module, and the full waveform from each channel over approximately 100 ms will be recorded on each beam pulse.

Nine modules will be placed just behind the absorber in a cross pattern. An additional 12 will be placed at multiple depths in the shielding in order to sample the muon flux from different energies, as shown in Figures 3.16. The shielding will simultaneously act to range out the muons and shield the detectors from neutrons. The Cherenkov light from Michel-decay electrons will exit the counter and be collected by either nearby PMTs or by a light guide which will guide the light to a remote optical sensor.

To probe the muon flux at lower energies, it may also be feasible and/or desirable to place some additional modules within the downstream part of the absorber or in the outermost radii of the decay-pipe shielding. The ability to do this may be limited, however, by the presence of muons from stopped, positively charged pion decays due to nearby hadron showers.

Besides the Michel decays of stopped muons, the system will independently measure both the μ^+ and μ^- stopped rates as a function of depth. While the 2.2 μs decay time of the μ^+ is a reliable signature, in mineral oil roughly 8.5% of the μ^- undergo capture on the ^{12}C nucleus, and 15% of those leave behind a ^{12}B ground state nucleus. That ^{12}B nucleus will undergo β decay with a half-life of 20.20 ms and an electron spectrum with an endpoint of 13 MeV. This signal is expected to yield a reliable measurement of the rate of stopped μ^-.

3.6.3 Prototype Development and Testing

Prototype development activity for the Michel-electron detectors will be divided into studies of the rate and radiation environment where the detectors will be located and development of the counters themselves.

The radiation environment will be studied both with Monte Carlo simulations and by measurements from initial prototype detectors in the NuMI muon alcoves [3]. The prototypes will be installed into the alcoves in 2016 and 2017. Studies will be performed to determine if the photon

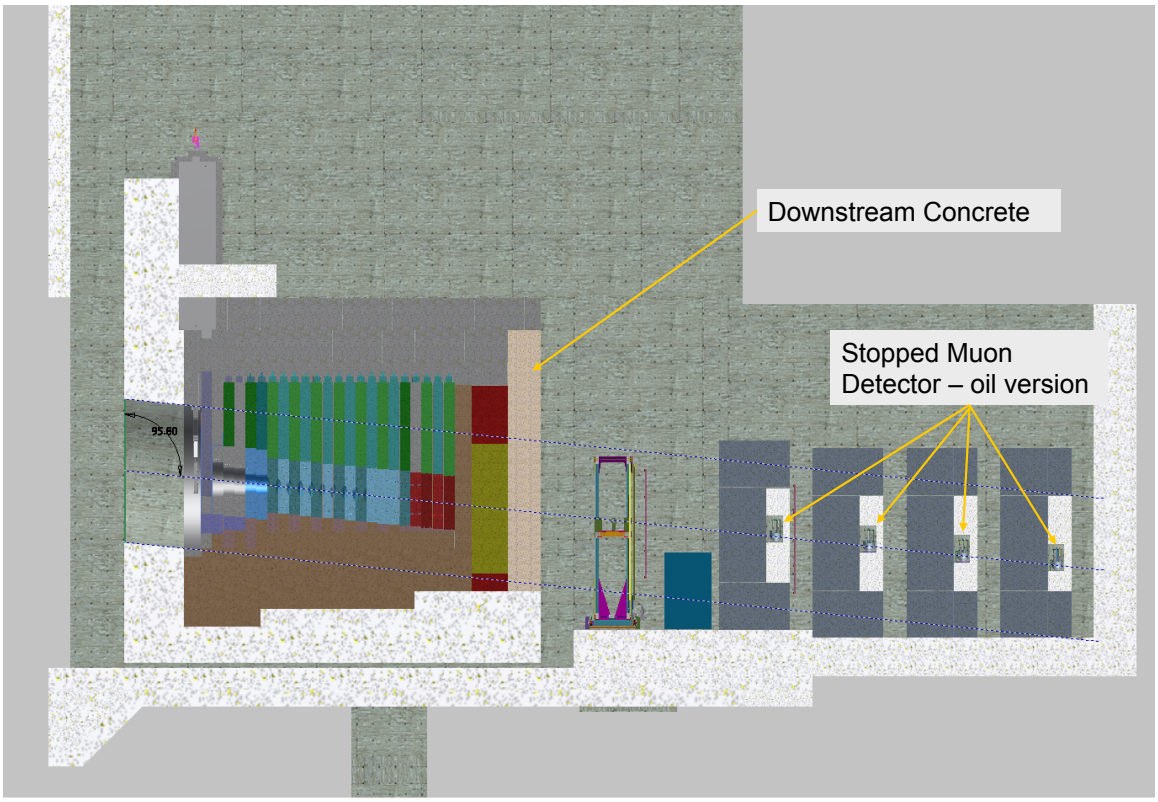

Figure 3.16: Stopped muon counter conceptual design. The figure shows the elevation view of the absorber at the end of the decay tunnel along with the locations of a subset of the stopped muon counters, and showing a possible arrangement of "blue blocks" and stopped muon detectors. In this case there is roughly 2 GeV of energy loss per wall of blue blocks. The final arrangement is under investigation and will depend on the final absorber design.

sensors can survive the radiation environment at the location of the Michel detector. If the sensors can survive, they can be attached directly to the Cherenkov medium; if not, optical guides will have to bring the light to a lower-radiation area to the side of the beam. Potential radiation damage to the Cherenkov radiator itself will also be studied.

The detector design will focus on selecting radiator and shielding material, photon-detection technology and control/readout hardware. Possible radiators include aerogel, which may be designed to be replaced periodically, and flowing liquids such as H_2O or mineral oil. Long-timescale saturation from the very high-rate environment of the beam spill could affect the photon-counting devices [12]. Thus, it will likely be necessary to design fast-switching, high-voltage circuits that turn on the photon counters in the first few microseconds after the spill is over. A similar system was developed in the 1990s for the Brookhaven Muon (g-2) Experiment [13] .

3.6.4 Installation

The stopped-muon counters will be installed after completion of the Absorber Hall and LBNF 30 and installation of the absorber. They will be placed into the spaces between the blue-block walls on support frames. There will be access to the areas between the shield blocks from the side, and the stopped-muon counters will be designed so that they can be wheeled in from the side. If needed, they could then be moved around to measure the stopped-muon rates across the muon beam.

3.6.5 Operation

The muon-monitor-system data will be displayed in the control room on a spill-by-spill basis to monitor the beam stability. Because the system will be located in a radiation-controlled environment that will not be accessible during the beam operation, it is essential that the electronics be designed for remote operation.

Chapter 4

Data Acquisition and Computing for the Near Detector System

4.1 NDS DAQ

The Near Detector System (NDS) Data Acquisition system (NDS-DAQ) collects raw data from each NDS detector's individual DAQ, issues triggers, adds precision timing data from a global positioning system (GPS), and builds events. The NDS-DAQ is made up of three parts, as shown in the block diagram of Figure 4.1, a master DAQ and one each for the near neutrino detector (NND, which is the FGT) and the BLM systems. The names for these are, respectively, NDS-MDAQ, NND-DAQ and BLM-DAQ.

4.1.1 NDS Master DAQ

The NDS Master DAQ (NDS-MDAQ) is designed to provide a high-level user interface for local run control and data taking, as well as for secure remote control and monitoring. It will serve as the primary interface to the NND-DAQ and BLM-DAQ and will include the following:

- slow-control system
- online data and DAQ performance monitoring
- raw data collection
- building of events
- data storage.

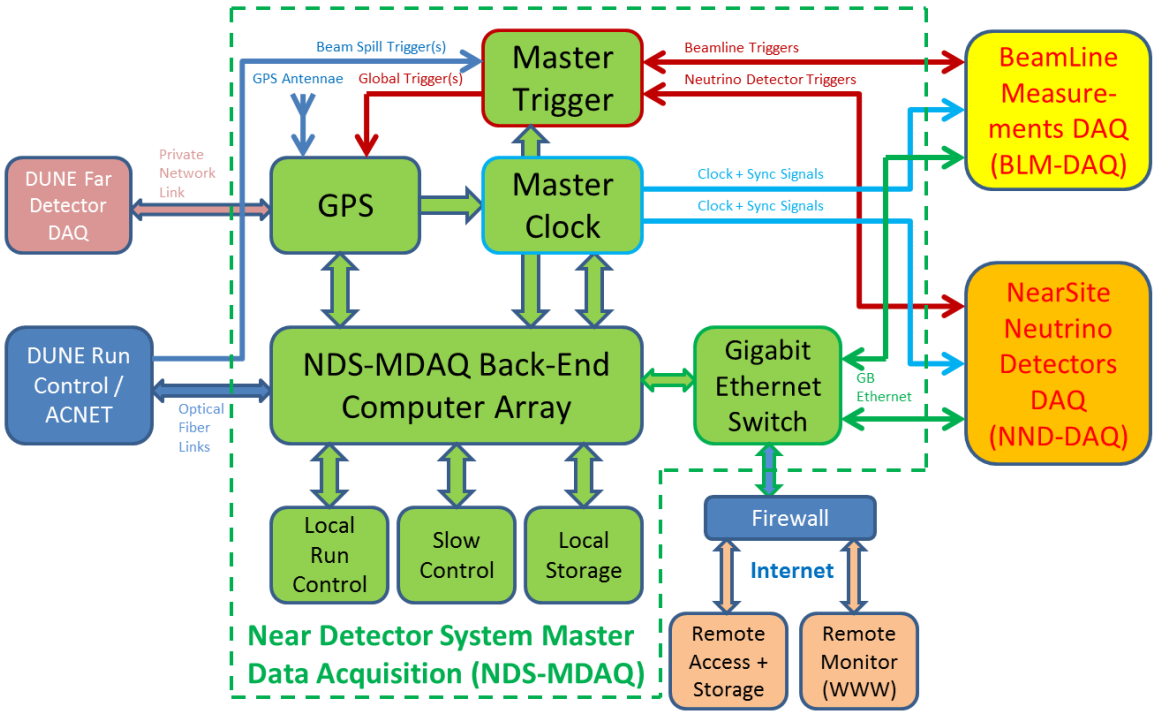

Figure 4.1: Near Detector System DAQ block diagram: The NDS-DAQ consists of the NDS Master DAQ (green blocks), the Beamline Measurement DAQ (yellow summary block) and the Near Neutrino Detectors DAQ (orange summary block). The NDS-DAQ connects to other portions of DUNE and LBNF, shown here in other colors (blue, light red, tan).

The NDS-MDAQ includes hardware two-way triggering for both the NND-DAQ and BLM-DAQ, and GPS hardware for precision time-stamping and global clock synchronization. The design is currently based on a channel count estimate of approximately 433,000 from the near neutrino detector, plus $< 1,000$ from the beamline detectors. Custom electronic components for the NDS-DAQ are based on existing custom designs from other experiments, e.g., T2K and ATLAS, and implement commercial components for the trigger modules, clock and timing synchronization, GPS and environmental monitoring.

4.1.2 Near Neutrino Detector DAQ (NND-DAQ)

The Near Neutrino Detector Data Acquisition system (NND-DAQ) collects raw data from the DAQ in each NND subdetector and connects to the NDS Master DAQ via Gigabit Ethernet. A block diagram of the NND-DAQ is shown in Figure 4.2. The NND-DAQ will mainly consist of a scalable back-end computer array, interconnected to the individual subdetector DAQs via Gigabit Ethernet, and specialized electronics modules for trigger processing and clock synchronization. It interfaces to the NDS-MDAQ for run control and data collection. The NND-DAQ will also have its own local run-control setup, consisting of a number of desktop workstations to allow independent local runs that include NND subdetectors only; this is useful during detector commissioning, calibration runs, stand-alone cosmic runs, or other runs where the beam is stopped or not needed.

The quantity of computers required for the NND-DAQ back-end system is highly dependent on the number of channels and expected data rates of the individual neutrino detectors. One back-end computer should be able to handle approximately 3,000 channels for sustainable and continuous runs. Assuming a total of 433,000 channels for all NND subdetectors combined, about 150 back-end computers would be needed.

Trigger signals from each subdetector will be collected and pre-processed by a trigger electronics module, similar in design to the NDS trigger or master-clock modules of the NDS-MDAQ design. Depending on the run mode, this module could feed local trigger decisions to the detector DAQs for data collection, or it could forward NDS triggers from the NDS-MDAQ or higher levels to the NND subdetector DAQs. A slave-clock electronics module, similar to the master-clock module in the NDS-MDAQ, distributes clock- and time-synchronization signals from the NDS-MDAQ to all NND subdetectors.

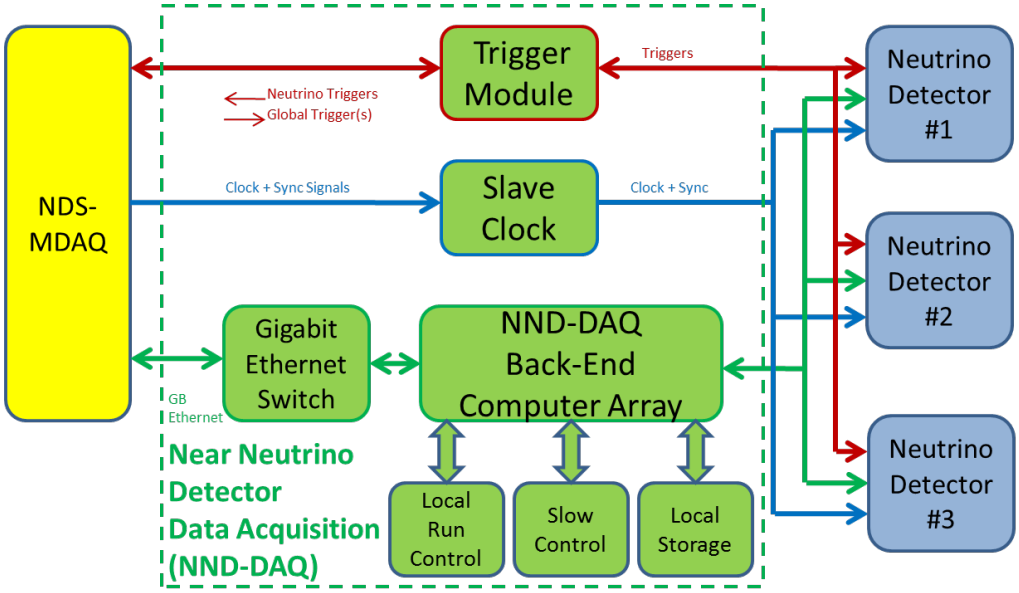

Figure 4.2: A block diagram of the Near Neutrino Detector DAQ (NND-DAQ).

4.1.3 Beamline Measurements DAQ (BLM-DAQ)

The BLM-DAQ will mainly consist of a scalable back-end computer array, inter-connected to the individual beamline measurement detector DAQs via Gigabit Ethernet and specialized electronics modules for trigger processing and clock synchronization. It interfaces to the NDS-MDAQ for run

control and data collection. It will also have its own local run-control setup, consisting of a number of desktop workstations to allow independent local runs that include beamline measurement detectors only; this is useful during detector commissioning, calibration runs, stand-alone cosmic runs or other runs where the beam is stopped or not needed.

4.2 NDS Computing

The computing system encompasses two major activities: online computing with required slow-control systems, and offline computing for data analysis and event simulation. The computing components are based on currently available commercial computing and gigabit networking technology, which is likely to improve over the next years without driving costs up for the final design.

Chapter 5

Measurements at External Facilities

5.1 Introduction

The technical components that would be needed to implement the strategies described in this chapter are outside the scope of the DUNE NDS conceptual design. This information is included in this document because it complements the conceptual design and expands the NDS capabilities to more closely meet the mission need without increasing the project cost.

5.2 External Neutrino-Beam Measurements

As discussed in Section 5.3.2, DUNE's strategy for neutrino-beam measurements includes making measurements of the Far Detector response to a known flux of neutrinos, and NuMI is the only appropriate beam line to use for the neutrino source.

To implement this strategy, appropriate detectors will need to be built. A plausible scenario would be a liquid argon TPC detector of 20-30 tons in the current location of the Minerva experiment, in front of the MINOS near detector. In that way, the MINOS near detector could be used to measure the charge of muons exiting the TPC. The TPC would be designed using the same readout technology that is used in the DUNE Far Detector. Once an optimal detector arrangement is determined, DUNE would use the same beam simulation and same muon measurements to apply that knowledge to the LBNF beam and Far Detector.

5.3 External Hadron-Production Measurements

Uncertainties on hadron production will translate into uncertainties in the neutrino fluxes in the DUNE Far Detector, since the neutrinos are produced by hadrons decaying in the decay pipe.

Precise calculations of neutrino fluxes in high-energy accelerator beams are limited at present by our knowledge of hadron production cross-sections in hadron-nucleus collisions. The modeling of strong-interaction cascades and hadronic yields from "thick" targets (up to a couple of interaction lengths) relies on detailed knowledge of underlying physics and cross-sections, which must be provided as a starting point to simulations. The resulting prediction of the flux of neutrinos, produced from decays of pions, kaons, and muons emerging from a hadronic shower and beam line re-interactions, is an essential part of simulations of most neutrino experiments.

Two-detector neutrino oscillation experiments predict the neutrino flux at the far detector by using neutrino fluxes "calibrated" (or appropriately scaled) by event energy spectra measured in the near detector. However, even these experiments must rely on the beam simulations since the decay pipe (where most beam neutrinos are created) provides different angular acceptance for the two detectors. In addition, experiments using near and far detectors based on different detection technologies further complicate the extrapolation. This chapter outlines the DUNE strategy for augmenting the capabilities of the BLM with external measurements of secondary-beam particles.

5.3.1 Background

A complete knowledge of the momenta and decay points of the kaons, pions and muons would be sufficient to completely predict the un-oscillated flux of neutrinos at the Near and Far Detector locations. This would require knowledge of:

- the phase-space distribution of the initial proton beam
- details of all materials present in the target, horn and decay pipe areas
- the electromagnetic focusing characteristics of the magnetic horn
- the detailed development of the hadron cascade, spawned by the initial proton, that passes through the target/horn/decay pipe
- the meson-to-neutrino decay rates

With careful engineering design and careful control of the materials in the target area, all of these items can be simulated accurately except hadronic cascades in the target, horn and decay pipe. The simulation of the hadronic cascade requires accurate knowledge of the hadron scattering cross sections, for which there are no first-principle calculations. These cross sections must therefore rely on models, which in turn require hadron-production measurements that span particle type, particle energy and the various materials found in the target, horn and decay pipe.

At the present time, a sufficient body of hadron-production measurements does not exist to achieve DUNE's desired accuracy of 4-5%, as determined by the irreducible error on the statistical uncertainty for the appearance-measurement back-ground, although this is expected to improve over time. As the BLM system described in Chapter 3 cannot meet this requirement alone, a near-far comparison will be more complicated than in certain other neutrino-oscillation experiments, e.g.,

MINOS experiment [2].

5.3.2 Strategy

The current approach is to rely on measurements made externally (outside the scope of DUNE) to calibrate detector response and flux simulations, and to relate these measurements to DUNE. This would be done through the use of a common simulation code and through measurements of tertiary muons in both DUNE and the external facility, using nearly identical tertiary muon-measurement systems.

In order to keep the uncertainty in the near/far event-rate ratio from being limited by systematic uncertainties in the flux, the DUNE flux simulation must be accurate at the 4-5% level. Efforts at this stage are intended to understand the effect of the uncertainties in hadron-production in the beamline on overall DUNE sensitivities, to determine what further measurements may be needed by DUNE and to estimate their potential cost to the Project.

The measurements that DUNE would require from an external facility begin with the primary hadron-production cross sections in the proton-target material, followed by similar studies in thick targets, and finally hadron yields after passage through the complete target and focusing-horn system. In addition, hadron-interaction cross sections on materials in the decay pipe and absorber can be important in flux calculations.

External hadron-production measurements are expected to play a critical role once the Far Detector has accumulated sufficient statistics toward the end of the running period to make systematic errors on the flux a dominant source of error in the oscillation measurement.

5.3.3 Use of External Facilities for Measurements

Historically, a number of hadron-production experiments have contributed directly to the outcome of neutrino experiments by measuring meson production from the proton targets used by those experiments, and hence providing a constraint on their neutrino fluxes. For example, the HARP data[14] contributed directly to MiniBooNE and the SPY[15] experiment contributed directly to NOMAD. Since their contributions were crucial to those neutrino experiments, it is also expected that DUNE will require some dedicated hadron-production measurements. In the future, the MIPP experiment at Fermilab is planning to contribute its measurements to the NOνA experiment, and the NA61 experiment [16, 17] is contributing to the T2K experiment [18].

A suitable apparatus for DUNE's hadron-production measurements is the collection of equipment and detectors used by the MIPP experiment at Fermilab [19]. A full suite of DUNE-related hadron-production measurements would require the installation of the DUNE horn-focusing elements and associated power supplies in front of a future incarnation of MIPP in the meson area at Fermilab. This kind of effort could be within the scope of the DUNE Project and could be postponed until after DUNE construction or even after DUNE operations have stopped.

5.4 The US-NA61/SHINE Program

A proposal to make measurements for the Fermilab neutron program with the NA61/SHINE experiment has been funded by DOE/HEP [20, 21] , US-NA61, and recommended by the CERN SPSC. NA61/SHINE is situated in the North Area of CERN on the H2 beam line.

The detector, schematically shown in Figure 5.1 is comprised of two large air gap, Helmholtz-coil superconducting magnets with a total bending power of 9 T-m. The detector is instrumented with gas TPC tracking, time-of-flight counters, and a hadron calorimeter (at very forward angles). The US-NA61 measurements will provide hadron-production data sufficient for predicting neutrino fluxes at DUNE. A pilot run of 120 GeV/c protons interacting on a thin 4% graphite target was taken by NA61 during July, 2012. A 4-week dedicated physics run is scheduled for October, 2015.

The run plan for the 2015 data is shown in the table in Figure 5.2. The initial run will focus on proton and pion data at 120 GeV/c and 60 GeV/c energies. This will constrain well extrapolations from higher and lower energies that are currently under use in neutrino beam simulations.

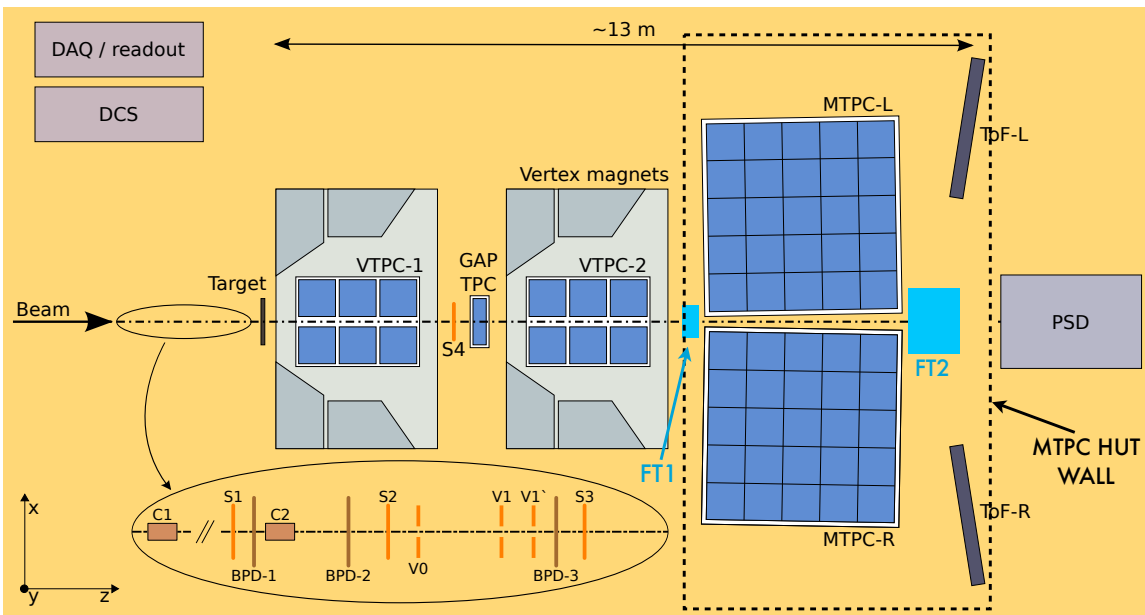

Figure 5.1: A schematic drawing of the CERN NA61 detector, a hadron production and heavy ion experiment designed to measure hadrons over a large part of the relevant phase for neutrino experiments. The TPCs, shown in blue, can separate pions from protons and kaons.

proton+pion event totals	Incident proton/pion beam momentum		
Target	120 GeV/c	60 GeV/c	30 GeV/c
NuMI (spare) replica	(*future*)		
LBNE replica	(*future*)		
thin graphite ($< 0.05\lambda_I$)	3M	3M	(T2K data)
thin aluminum ($< 0.05\lambda_I$)		3M	(*future*)
thin steel ($< 0.05\lambda_I$)	(*future*)	(*future*)	(*future*)
thin beryllium ($< 0.05\lambda_I$)	3M	3M	(*future*)

Figure 5.2: A table that shows the proposed run plan for the US-NA61 data run in the fall of 2015.

References

[1] "Near Detectors Requirements Documentation," tech. rep., 2012. LBNE Doc 5579 http://lbne2-docdb.fnal.gov:8080/cgi-bin/ShowDocument?docid=5579.

[2] MINOS Collaboration, "Measurement of Neutrino Oscillations with the MINOS Detectors in the NuMI Beam," *Phys.Rev.Lett.*, no. 101:131802, 2008.

[3] S. Kopp *et al.*, "Secondary beam monitors for the NuMI facility at FNAL," *Nucl. Instrum. Meth.*, vol. A568, pp. 503–519, 2006.

[4] "GNUMI NuMI Beamline Simulation Code." http://www.hep.utexas.edu/numi/beamMC/MC-code.html.

[5] "Cividec Diamond Detector," 2014. http://cividec.at/Diamond_Detectors_B10_Cryogenic_Diamond_Detector.html.

[6] M. H. Ahn *et al.*, "Measurement of Neutrino Oscillation by the K2K Experiment," *Phys. Rev.*, vol. D74, p. 072003, 2006.

[7] T. Maruyama, *First Observation of Accelerator Origin Neutrino Beam After Passing Through 250km of Earth.* PhD thesis, Tohuku University, 2000.

[8] K. Matsuoka *et al.*, "Development and production of the ionization chamber for the T2K muon monitor," *Nucl. Instrum. Meth.*, vol. A623, pp. 385–387, 2010.

[9] H. Kubo *et al.*, "Development of the muon beam monitor for the T2K Long Baseline Neutrino Oscillation experiment," *2008 IEEE Nuclear Science Symposium Proceedings*, pp. 2315–2318, 2008.

[10] D. Meier *et al.*, "Proton irradiation of CVD diamond detectors for high-luminosity experiments at the LHC," *Nucl. Instrum. Meth.*, vol. A426, p. 173, 1999.

[11] K. Hiraide, "Muon Monitoring Using the Decay Electrons," in *4th Workshop on Neutrino Beams and Instrumentation (NBI2003)*, 2003.

[12] Y. Semertzidis and F. Farley, "Effect of light flash on photocathodes," *Nucl. Instrum. Meth.*,

vol. A394, p. 7, 1997.

[13] J. Ouyang and W. Earle, "Muon g-2 note no. 202," tech. rep., BNL, 1994.

[14] M. Catanesi *et al.*, "Measurement of the production cross-section of positive pions in p-Al collisions at 12.9-GeV/c," *Nucl.Phys.*, vol. B732, pp. 1–45, 2006.

[15] G. Ambrosini *et al.*, "Pion yield from 450-GeV/c protons on beryllium," *Phys.Lett.*, vol. B425, pp. 208–214, 1998.

[16] N. Abgrall *et al.*, "Measurements of Cross Sections and Charged Pion Spectra in Proton-Carbon Interactions at 31 GeV/c," *Phys.Rev.*, vol. C84, p. 034604, 2011.

[17] N. Abgrall *et al.*, "Measurement of Production Properties of Positively Charged Kaons in Proton-Carbon Interactions at 31 GeV/c," *Phys.Rev.*, vol. C85, p. 035210, 2012.

[18] K. Abe *et al.*, "T2K neutrino flux prediction," *Phys.Rev.*, vol. D87, no. 1, p. 012001, 2013.

[19] D. Isenhower *et al.*, "Proposal to upgrade the MIPP experiment," *unpublished*, 2006. hep-ex/0609057.

[20] "Study of Hadron Production in Hadron-Nucleus and Nucleus-Nucleus Collisions at the CERN SPS; CERN-SPSC-2006-034," 2006. `http://cds.cern.ch/record/995681?ln=en`.

[21] "Hadron Production Measurements for Fermilab Neutrino Beams: CERN-SPSC-2014-032," 2014. `https://cds.cern.ch/record/1955140/files/`.